# The impact of high-frequency atmospheric forcing on the Yellow Sea Warm Current and warm salty water intrusion in the Southern Yellow Sea

Yang Ding[1*], Xianwen Bao[1,2], Zhigang Yao[2], Congcong Bi[2], Guandong Gao[3], Xueming Zhu[4], Jinyong Choi[5], Lingling Zhou[2], Zhiyi Gao[4]

[1]*Physical Oceanography Laboratory/CIMST, Ocean University of China and Qingdao National Laboratory for Marine Science and Technology, Qingdao, China*

[2]*College of Oceanic and Atmospheric Sciences, Ocean University of China, Qingdao, China*

[3]*Key Laboratory of Ocean Circulation and Waves, Institute of Oceanology Chinese Academy of Sciences, Qingdao, China*

[4]*Key Laboratory of Research on Marine Hazards Forecasting, National Marine Environmental Forecasting Center, Beijing, China*

[5]*Marine Disaster Research Center,Korea Institute of Ocean Science and Technology, Busan, Republic of Korea*

**Key Points:**

1) Synoptic fluctuation of the Yellow Sea Warm Current
2) Frequent storm burst and relaxation excite coastal trapped waves
3) High frequency weather systems affect the warm and salty water transport

*Corresponding author: Yang Ding
E-mail address: dingyangpol@ouc.edu.cn

# Abstract

The impact of high-frequency atmospheric forcing on the Yellow Sea (YS) circulation with emphasis on the Yellow Sea Warm Current (YSWC) was investigated by comparing model simulations with and without high-frequency atmospheric processes. By including the high-frequency atmospheric forcing at the synoptic scale in an atmosphere reanalysis used to force the ocean model, the simulated intensity of the mean YSWC is increased by 40-100%. The mean temperature is decreased by up to 1°C, and the mean salinity along the YSWC pathway is increased by up to 0.2-0.5 psu. Additional simulations in which either the wind or other atmospheric fields were filtered revealed that the high-frequency wind forcing is more important in the YSWC and relates mean temperature with the other atmospheric variables that play relatively minor roles. In winter, the high-frequency wind forcing associated with frequent winter storm bursts and relaxation is able to excite coastal trapped waves propagating cyclonically around the Bohai Sea and Yellow Sea coast; this forcing is a very important factor influencing the synoptic variability in the YSWC and drives intermittent warm and salty water intrusion into the southern YS. The results from this study provide a basis for a new understanding of how transient atmospheric phenomena, such as winter storms, impact regional circulation and water transport in the YS.



**Plain language Summary**

The Yellow Sea Warm Current (YSWC) is one of the most important phenomena in

the Yellow Sea. It is the only open ocean water from Kuroshio origin flowing into the Yellow Sea interior under prevailing northwesterly monsoon during winter season. Since the YSWC transports water with obvious high temperature and salinity, the intensity and variations of the YSWC have a crucial effect on the regional circulation and biogeochemistry in Yellow Sea and also effects the sea ice coverage in the Bohai Sea. Direct observations reveal that the high-frequency variations of the atmospheric forcing associated with frequently occurred winter storm bursts affect the YSWC significantly. Using a numerical ocean model, we evaluate the effect of the high-frequency atmospheric forcing on the YSWC. We show that including high frequency atmospheric forcing at synoptic scale is able to increase the simulated intensity of the mean YSWC by up to 40-100%. This study provides a base for new understanding of how the transient atmospheric phenomena such as winter storms impact the reginal circulation in shelf seas.

## 1. Introduction

The surface wind forcing is strongly dependent on day-to-day weather phenomena (Duteil, 2019). Neglecting high-frequency winds can induce large errors in estimating surface wind stress (Esbensen and Reynolds, 1981; Gulev, 1994). According to Zhai (2013), including high-frequency wind fluctuations in the stress calculation significantly modified the mean wind stress estimates. The power input to the ocean general circulation increases by more than 70% if synoptic winds are considered in the stress calculation, especially in regions of mid and high latitudes

where synoptic wind activity is prominent (Zhai et al., 2012).

In recent studies, high-frequency atmospheric forcing on the synoptic time scale has been recognized as very important in regulating ocean circulation, heat transport and oxygen levels (Zhai, 2012; Wu et al., 2016; Munday and Zhai, 2017; Duteil, 2019). In the Southern Ocean, strongly varying atmospheric wind is considered to strengthen the near-surface viscous and diffusive mixing, which leads to a thicker mixed layer and higher sensitivity of the residual circulation (Munday and Zhai, 2017). By comparing simulations of a global model forced with and without synoptic atmospheric phenomena, Wu et al. (2016) showed that the wind-driven subtropical gyre circulations were strengthened by approximately 10%-15% and the maximum global northward heat transport increased by nearly 50% if synoptic atmospheric forcing was included in the model. Similarly, the intensity of the Atlantic meridional overturning circulation and subpolar gyres tended to decrease by 25% if high-frequency atmospheric forcing was excluded in a coupled ocean-ice model (Holdsworth and Myers, 2015). Chen et al. (1999) evaluated the effects of wind forcing temporal smoothing in a model simulation and found that the mean sea surface temperature (SST) increased by 0.5°C to 1°C over most of the tropical Pacific when the daily wind forcing was replaced by monthly mean data. Using a one-dimensional mixed-layer model for the central Arabian Sea, Zhou et al. (2018) found that the daily mean SST was lowered by 0.8°C on average when including high-frequency signals in the meteorological variables. Based on a global ocean model, Duteil (2019) removed the higher frequency variability of wind (2 days to 1

103 month) used to force the ocean model and revealed that the wind stress was decreased
104 by 20% in the tropics and 50% in the midlatitudes. Consequently, the wind-driven
105 circulation was weakened by up to 20%. Correspondingly, the oxygen levels
106 decreased by up to 10 mmol/$m^3$ in the tropical oceans and 30 mmol/$m^3$ in the
107 subtropical gyres, which was mainly caused by modification of advective processes
108 related to the change in wind forcing. Furthermore, the high-frequency information of
109 the wind forcing is very important for river plume simulations in coastal oceans, and
110 the simulation error is regarded to be closely related to the subsampling of
111 high-frequency wind (Qu and Hetland, 2019). Therefore, high-frequency atmospheric
112 forcing plays a crucial role in ocean circulation at multiple scales from the estuary to
113 the global ocean.

114 The Yellow Sea (YS) and Bohai Sea (BS) are shallow semienclosed shelf seas
115 (Fig. 1). In the BS and YS (Fig. 1), synoptic weather systems with frequencies
116 ranging from 2 to 10 days are very prominent, especially during winter. The main
117 source of synoptic variability in winter is northerly storm wind bursts, often
118 displaying high wind speeds exceeding 20 m/s. During winter, strong atmospheric
119 frontal systems associated with winter storms usually strike the BS and YS from north
120 to south (Hsueh and Romea, 1983; Hsueh, 1988; Yin et al., 2014). These
121 high-frequency weather systems cause the wind speed to fluctuate significantly at
122 synoptic time scales of 2-7 days.

123 The regional circulation in the YS during winter is mostly driven by wind. A
124 northward current flowing against the winter wind is known as the Yellow Sea Warm

Current (YSWC). The YSWC is the most important phenomenon in the YS during winter. The YSWC is considered to have a crucial effect on the circulation and biochemistry in the YS and BS (Lie et al., 2009; Su et al., 2005; Liu et al., 2015), as it is the only current that transports warm saline water into the YS from the Kuroshio origin (Lie et al., 2009; Lin et al., 2011; Lie and Cho, 2016). Previous observations in the YS indicate that high-frequency atmospheric forcing, such as winter storms, has the potential to induce a quick oscillation of the YSWC on the synoptic scale (Ding et al., 2018), which is effective for cross-front sediment transport in the northern YS (Shi et al., 2019) and warm saline water transport in the southern YS (Lie et al., 2013; Lie et al., 2015; Pang et al., 2016; Ding et al., 2018). Direct current observations in both the northern and southern YS during the winter of 2007 show significant synoptic fluctuations in the YSWC (Yu et al., 2010; Ding et al., 2018), which were considered to be related to synoptic wind forcing. However, how these synoptic atmospheric systems associated with frequent winter storms affect the YSWC and the related warm salty water transport remains unclear.

To the best of our knowledge, very few studies have investigated the effect of these high-frequency weather systems on YS circulation, especially on the YSWC. Therefore, in this study, we are investigating how the high-frequency atmospheric forcing, or in other words, the integrated impact of day-to-day weather systems, affects the regional circulation in the YS with a particular focus on the YSWC during winter. Numerical ocean models provide us with a useful tool to increase our ability to explore the role of high-frequency atmospheric processes in regional ocean processes.

147 Thus, we attempt to evaluate the important effect of high-frequency synoptic weather
148 systems on the YSWC by comparing model simulations with and without
149 high-frequency atmospheric processes.

150 This paper is organized as follows. We begin in section 2 with a description of the
151 observations and model experiments. The impact of synoptic atmospheric forcing on
152 the time-averaged quantities of the YSWC is described and discussed in section 3. We
153 discuss the relative roles of high-frequency wind and other atmospheric fields in
154 modeling the temperature of the YSWC and examine the effect of high-frequency
155 variations in wind on the warm saltwater intrusion into the southern YS in section 4.
156 We conclude with a summary of our results in section 5.

157 ## 2. Data and model experiments

158 2.1 Observational data

159 To observe the YSWC, two current moorings with bottom mounted ADCP were
160 deployed in the southern YS along the 70 m depth contour from January to March
161 2017 (blue triangular in Fig. 1). Since the synoptic variability in the YSWC is closely
162 correlated with the subtidal sea level fluctuations, we also collected sea level
163 observations from 16 coastal tide gauge stations along the BS and YS coasts (red dots
164 in Fig. 1) during winter and spring 2017. The time series of sea level anomalies were
165 lowpass filtered to remove tidal signals. Fig. 2 (a) shows the observed lowpass filtered
166 sea level fluctuations at the 16 coastal tide stations. Significant sea level fluctuations
167 at synoptic time scales ranging from 2-5 days can be noted at all tide gauge stations,
168 especially during January and February. Very sharp sea level decreases associated

with winter storms occasionally occurred. The maximum sea level decrease exceeded 1 m. After February, severe weather events became rare, and the wind tended to become weak. Correspondingly, the sea level fluctuations became weak, and no significant sea level decrease was observed.

The time-distance contour of the sea level anomaly at the coastal tide stations along the YS and BS coast is presented in Fig. 2(b). It is clear that prominent negative sea level anomalies mainly occurred in the winter months of January and February. Negative sea level anomalies are often followed by positive sea level anomalies throughout the winter season. The tilt of contours of the positive and negative sea level anomalies suggests cyclonic propagation of sea level signals around the BS and YS coast with a period of 2-5 days, which can be more clearly seen in the enlarged view shown in Fig. 2(c), which focuses on the time during February. Lag correlations were applied to the selected station pairs along the BS and YS coasts. We avoid choosing stations that are too close to each other because these stations may reach the maximum or minimum sea level simultaneously. Table 2 lists the correlation coefficients and lag times between the selected stations and MokPo station. The correlation coefficients are all greater than 0.7 above the 95% confidence level. The lag time gradually increases from 1 hour to 23 hours. The lag correlation of subtidal sea level anomalies indicates that a phase propagation exists along the coast. Analysis of the sea level anomaly in Ding et al. (2019) has also revealed that the propagation of sea level signals is from trapped coastal waves induced by periodic winter storm bursts.

Fig. 3 shows the observed subtidal current at mooring locations M1 and M2 during the 2017 winter cruise. The significant synoptic variability in the subtidal current can be noted at both M1 and M2. A strong northward current with a maximum magnitude exceeding 15 cm/s occurred intermittently during the observational period, which indicates that the prominent YSWC was also captured by the two moorings. The northward YSWC was often interrupted by storm-induced southward currents, especially during the winter months of January and February. A strong northward YSWC burst usually occurred after the southward current. Comparing the observed subtidal current in Fig. 3 and sea level fluctuations shown in Fig. 2, we can see that a prominent northward YSWC burst tended to appear during January and February when a sharp sea level decrease frequently occurred. The observed significant oscillations in sea level and subtidal current suggest that the BS and YS were under frequent influence of synoptic weather events during winter and early spring 2017. The high-frequency atmospheric forcing associated with frequent storms is also able to excite episodic spikes in the YSWC.

## 2.2 Reanalysis atmospheric data

The atmospheric data were obtained from the National Centers for Environmental Prediction (NCEP) Climate Forecast System Version 2 (CFSv2). The surface atmospheric data at one-hourly intervals, including surface wind, longwave and shortwave radiation, air temperature, sea level pressure, precipitation and evaporation, and relative humidity, were used to force the ocean model. The hourly atmospheric forcing data used here can better resolve a wide range of weather

phenomena.

Fig. S1 shows the time series of surface wind, air temperature and sea level pressure averaged in the 121-126°E and 31-36.5°N region covering the southern YS from January to April. Clearly, the synoptic fluctuations in the atmospheric variables are very prominent during January and February. The northerly storm burst with a maximum wind speed exceeding 15 m/s occasionally occurred (Fig. S1a). The strong northerly wind usually lasted for 2-3 days and then relaxed and sometimes even reversed to a strong southerly or southwesterly wind. Simultaneously, the air temperature and air pressure featured sharp increases and decreases, which is also related to multiple storms during winter 2017.

2.3 Numerical model and experimental design

Both the observed sea level fluctuations at tide stations along the coast and subtidal currents at two moorings west of the YS trough show significant synoptic fluctuations during the 2-3 day period in winter and early spring. The synoptic fluctuations are mainly related to the high-frequency wind forcing. To evaluate the effect of high-frequency atmospheric forcing on the YSWC, numerical ocean modeling was conducted. The numerical ocean circulation model used here is based on the Finite Volume Community Ocean Model (FVCOM, Chen et al. 2003, 2007). The configuration encompasses the region of 21°-41°N, 117°-138°E, which covers the whole BS, YS, and East China Sea (ECS) with three open boundaries: one boundary crossing Taiwan Street, one in the northwest Pacific Ocean and another boundary crossing the Japan Sea (blue dashed line in Fig. 1). This model has been

used to investigate the synoptic variation in the YSWC during winter 2007 (Ding et al., 2018) and synoptic current fluctuations in the Bohai Strait during winter 2017 (Ding et al., 2019).

The model's highest horizontal resolution was approximately 1-2 km around the coastal region in the BS and YS. The lowest resolution is approximately 20 km near the open boundaries. The configuration has 30 vertical levels with uniform sigma layers. The atmospheric forcing data in the model were taken from one-hourly data of NCEP/CFSv2 (https://rda.ucar.edu/datasets/ds094.1/), which includes one-hourly 10-m wind velocity, air pressure reduction to mean sea level, 2-m air temperature, relative humidity, precipitation and evaporation, downward longwave radiation, and net shortwave radiation. The surface latent and sensible heat fluxes are calculated based on bulk formulation (Fairall et al., 1996). For the lateral open boundary conditions, the sea surface height (SSH), velocity, temperature and salinity obtained from the global model of Estimating the Circulation and Climate of the Ocean Phase II (ECCO2, Menemenlis et al., 2008, http://apdrc.soest.hawaii.edu/data/data.php) at a 0.25°×0.25° resolution were applied along the open boundaries. In addition, the tidal forcing based on nine tidal constituents ($M_2$, $S_2$, $N_2$, $K_1$, $O_1$, $Q_1$, $M_4$, $MS_4$ and $MN_4$) derived from TPXO 7.2 (Egbert and Erofeeva, 2002, http://volkov.oce.orst.edu/tides/otis.html) was also used to drive the model. No temperature or salinity restoration is applied in the model configuration. The model bathymetry was interpolated from a combination of DBDB5 (US Naval Oceanographic Office, 1983) and depth data from China's coastal sea chart database.

Three main rivers, including the Changjiang River, Huanghe River and Liao River, were also included in the model to provide monthly mean freshwater discharge, which was obtained from the Information Center of Water Resources (Bureau of Hydrology, Ministry of Water Resources of P. R. China, http://www.mwr.gov.cn/sj/tjgb/zghlnsgb/).

The initial conditions for temperature and salinity are taken from ECCO2 on January 1, 2014. The initial velocity field and SSH are set to zero. The model was run as a spin-up simulation from 2014 to 2016 and continued to run from January to March 2017. The model results were compared with the observations to evaluate the model's performance. The model validation of sea level fluctuations, subtidal currents, temperature and salinity are shown in the appendix.

To explore the impact of the high-frequency atmospheric forcing on the YSWC, a control simulation and two sensitivity model experiments are conducted (Table 1). The control experiment (Exp-1HR) is forced by one-hour atmospheric data taken from NCEP/CFSv2. To isolate the impact of the synoptic atmospheric forcing on the YSWC, we conducted two perturbation experiments (Exp-7DAY and Exp-MON). The original NCEP/CFSv2 dataset used in the control run is characterized by a 1-hour time resolution. In the two experiments, we excluded synoptic atmospheric phenomena by performing a 7-day running mean (Exp-7DAY) and monthly averaging (Exp-MON) on the atmospheric variables (e.g., air temperature, sea level pressure, surface winds, relative humidity, longwave and shortwave radiation) prior to calculating the surface wind stress and heat flux. The

differences between the control run (EXP-1HR) and two sensitivity experiments (Exp-7DAY and Exp-MON) could highlight the impact of the high-frequency atmospheric forcing on the YSWC.

Three additional experiments were designed to separate the contributions of winds from the other atmospheric factors. In experiment Exp-WIND-MON, high-frequency signals are removed from wind by monthly average with the other atmospheric factors left intact for Exp-1HR, and vice versa for experiment Exp-HEAT-MON, i.e., high-frequency signals are removed for all atmospheric factors except for surface winds. The net heat flux into the ocean surface is determined by the bulk formulas in Exp-WIND_MON and Exp-HEAT-MON, meaning that the heat flux could be affected by any changes in either winds or other atmospheric factors. To isolate only the momentum aspect, an additional experiment of Exp-WIND-MON-HEAT-SET is considered, where the heat flux is prescribed at hourly intervals from the bulk formula calculation of the control run when momentum flux is determined from the monthly wind components. The difference between Exp-WIND-MON-HEAT-SET and Exp-1HR could highlight the role of momentum flux in the band of only high frequency.

Details of the sensitivity experiment settings are given in Table 1. All experiments, including the control run, were spun up for three years before validation and analysis for our observational period from January to March 2017. Hourly model output is saved for the following analysis.

## 3. Results

301 **3.1 Air-sea fluxes**

302 **3.1.1 Momentum flux**

303 The wind stress in the FVCOM is calculated following Large and Pond
304 (1981):

305 $$\overrightarrow{\tau_s} = C_d \rho_a \left|\overrightarrow{V_w}\right| \overrightarrow{V_w} \qquad (3.1)$$

306 where $\tau_s$ is the surface wind stress vector, $\rho_a$ is the air density, $V_w$ is the surface wind
307 speed, and $C_d$ is the drag coefficient, which is defined as follows:

308 $$C_d \times 10^3 = \begin{cases} 1.2 & \left|\overrightarrow{V_w}\right| \le 11.0\ m/s \\ 0.49 + 0.065\left|\overrightarrow{V_w}\right| & 11.0\ m/s \le \left|\overrightarrow{V_w}\right| \le 25.0\ m/s \\ 0.49 + 0.065 \times 25 & \left|\overrightarrow{V_w}\right| \ge 25.0\ m/s \end{cases} \qquad (3.2)$$

309 The wind stress depends quadratically on the wind speed, as denoted by the above
310 equation, and therefore, the nonlinearities have a great effect on the wind stress
311 calculation. Moreover, the drag coefficient for the wind stress calculation depends on
312 the magnitude of wind speed. As a result, high-frequency wind speeds, such as
313 synoptic weather systems, contribute significantly to the time-mean wind stress. In
314 Exp-7DAY and Exp-MON, the higher frequencies of the zonal and meridional wind
315 velocities have been removed. Removing the high frequencies of zonal and
316 meridional wind velocity affects the wind speed and then impacts the wind stress,
317 which ultimately dominates the intensity of ocean circulation.

318 The mean surface wind stress over the period from January to March from the
319 control run (Exp-1HR) is shown in Fig. 4a; the model differences between Exp-7DAY
320 (Exp-1HR minus Exp-7DAY) and Exp-MON (Exp-1HR minus Exp-MON) are shown
321 in Fig. 4b and c, respectively. The northerly and northwesterly winds prevail in the

322 entire BS and YS. The wind is relatively stronger in the eastern YS, while the BS and
323 western YS are mainly driven by weaker northerly winds. The magnitude of wind
324 stress reaches 0.1 pa in the eastern YS and decreases to 0.02-0.06 pa in the western
325 YS. Although the spatial patterns of the time-mean wind stresses are similar among
326 the three experiments (not shown), the magnitudes are greatly reduced in Exp-7DAY
327 and Exp-MON, particularly in the eastern YS. In the coastal region of the western YS,
328 where the magnitude of wind stress is lower, the differences among the wind stresses
329 in the three experiments are generally small. The intensity of wind stress over the
330 southern YS region (121°-126°E, 31°-37°N) is dramatically reduced by a fraction of
331 50% for Exp-7DAY, from 0.046 to 0.023 N $m^{-2}$, and by more than 60% for Exp-MON,
332 from 0.046 to 0.017 N $m^{-2}$.

333 Fig. 4 d and e show the time series of domain-averaged wind stress for the
334 three experiments from January to March 2017. Despite the fact that the mean spatial
335 pattern was very similar for both the filtered and unfiltered surface wind forcing, there
336 are significant differences between the time series with and without synoptic
337 fluctuations. In particular, the extrema of wind stress have been filtered when the
338 synoptic wind variability is removed. A comparison of the time series between the
339 filtered and unfiltered wind stresses also confirms that Exp-1HR has many more days
340 with extreme weather systems than Exp-7DAY. The figure clearly shows that the
341 strongest wind stresses often occur over a very short time scale, and the
342 high-frequency wind stress perturbations have been removed in Exp-7DAY and
343 Exp-MON. The extrema of wind stress have also been filtered when synoptic wind

variability is removed. The wind stress reaches 0.42 pa in Exp-1HR. However, in the filtered time series, the maximum wind stress only reaches 0.1 pa in Exp-7DAY, as demonstrated by the black and red lines in Fig. 4d-e.

### 3.1.2 Surface heat flux

The time-mean net surface heat flux in Exp-1HR is shown in Fig. 5a, and the differences (Exp-1HR minus Exp-7DAY and Exp-1HR minus Exp-MON) are shown in Fig. 5b-d. Removing the high frequencies of atmospheric variables modulates the latent and sensible flux and therefore impacts the surface net heat flux. Notably, the magnitude of net surface heat flux was reduced after removing the high-frequency phenomena from the atmospheric variables. The intensity of heat loss was decreased in Exp-7DAY and Exp-MON. After averaging over the southern YS, exclusion of the synoptic atmospheric forcing decreased the surface heat loss from ~68 W $m^{-2}$ in Exp-1HR to ~44 W $m^{-2}$ in Exp-7DAY and to ~37 W $m^{-2}$ in Exp-MON. The unfiltered and filtered time series for the net surface heat flux are shown in Fig. 5f. Similar to the comparison of wind stress, high-frequency atmospheric variables contribute significantly to the net surface heat flux. The time series of heat flux is smoothed, and the extrema are filtered out when ignoring the synoptic fluctuations of the atmospheric variables. Notably, the surface heat flux in the three model runs depends on the model-simulated SST, and changes in the regional circulation may also influence these differences in the net surface heat flux.

## 3.2 Time-averaged quantities of the YSWC

The control run and sensitivity experiments show the important role of

366 high-frequency atmospheric forcing in modulating the YS circulation. The model-data
367 comparison shown in the appendix also suggested that the model results agree well
368 with the observations when driven by the high-frequency atmospheric forcing. In this
369 section, we first examine the time-mean characteristics of the model simulations. The
370 comparison of the simulated time-mean current between Exp-1HR and Exp-MON is
371 shown in Fig. 6. The differences in the mean velocity (Exp-1HR minus Exp-MON)
372 also overlap in the figure. The comparison of the simulated time-mean current
373 between Exp-1HR and Exp-7DAY is shown in Fig. S2. The overall patterns of the
374 time-mean circulation in Exp-1HR, Exp-7DAY and Exp-MON are very similar. All
375 simulations reproduced the mean pattern of the winter circulation in the YS. The
376 time-mean currents in the three model experiments all show southward currents in the
377 eastern YS from the surface to the bottom and northward currents in the western YS
378 mainly in the subsurface and bottom layers. The northward current with a magnitude
379 ranging from 5~10 cm $s^{-1}$ in the lower layers is mainly located between the 50 and 70
380 m isobaths, which is the YSWC (Fig. 6 d-i). An anticyclonic gyre dominates the YS
381 basin in the subsurface and bottom layers, with a stronger northward YSWC along the
382 western trough of the YS and weaker southward current along the eastern shelf of the
383 YS. The simulated anticyclonic circulation pattern is similar to that shown in previous
384 studies (Takahashi et al., 1995; Moon et al. 2009; Lie and Cho, 2016). A branch of the
385 YSWC extending northwestward to the Shandong Peninsula at 34N$^{o}$, which was
386 proposed in previous studies (Ma et al., 2006; Wang et al., 2012), can also be noted.
387 A comparison of the time-mean current shows that including the

high-frequency variations in the atmospheric variables does not change the pattern of the mean current. However, the simulated horizontal circulation in the YS increases in strength. For example, the magnitude of the southward Korean coastal current in the surface layer and northward YSWC in the lower layers are greatly enhanced after including the high-frequency atmospheric forcing (Fig. 6b, d, f). The anticyclonic circulation in the central BS is also strengthened by a similar amount (Fig. 6a, b). The difference in the mean current in the lower layers (30 m and 50 m) between Exp-1HR and Exp-7DAY and Exp-MON is mainly limited along the YSWC pathway. In the lower layers (30 m and 50 m), the YSWC increases much more in strength than the southward Korean coastal current and the northwestward branch of the YSWC. The mean strength of the current along the YSWC pathway is increased by 40~100% when the high-frequency atmospheric forcing was considered in Exp-1HR compared with Exp-7DAY and Exp-MON. The strengthened surface wind stress owing to contributions from the high-frequency wind speed (Fig. 4) leads to a stronger current in the eastern YS in the surface layer (Fig. 6b). Thus, the northward YSWC is strengthened in the lower layers due to the effect of compensation (Fig. 6d, f), which agrees with the well-accepted mechanism raised in previous studies (Hsueh, 1988; Lie, 1999; Lin et al., 2011). These differences in the mean current are mainly attributable to the much stronger wind stress in Exp-1HR than in Exp-7DAY or Exp-MON.

The differences in model-simulated mean temperatures between the control run (Exp-1HR) and experiments (Exp-MON and EXP-7DAY) are shown in Fig. 7 and Fig. S3, respectively. The model captures the temperature structure in the YS well. The

410 warm tongue extending northward mainly along the YSWC pathway is well resolved
411 (Fig. 7a, d, g). The temperature patterns for the two experiments are very similar to
412 those from the control run, but the simulated mean temperature from the surface to the
413 bottom layers is decreased when including the high-frequency atmospheric forcing
414 (Fig. 7, c, f, i). We should note that the decrease in the mean temperature along the
415 YSWC pathway is relatively smaller than that in other regions, such as coastal areas.
416 For example, the temperature decrement is approximately 1°C in the central YS and
417 exceeds 3°C around the coastal regions of both the western and eastern YS. Based on
418 the temperature equation (Ma et al., 2006), the local temperature change can be
419 estimated as follows:

$$\frac{\partial T}{\partial t} = -\left(U\frac{\partial T}{\partial x} + V\frac{\partial T}{\partial y}\right) + F_T + \frac{Q}{\rho C_p h}$$

420 where $F_T$ is the horizontal turbulence diffusivity, $Q$ is the surface net heat flux and $h$ is
421 the water depth. It can be noted from the temperature equation that the temperature
422 change is smaller in the middle YS due to greater water depth. On the other hand, the
423 stronger YSWC in Exp-1HR tends to bring warmer water northward due to the
424 enhanced advection process in association with the high-frequency wind forcing.

425 There are also some differences between the mean salinity in the three
426 experiments (Fig. 8 and Fig. S4). It is clear that the mean salinity is increased by
427 0.2-0.5 psu in Exp-1HR compared with the two experiments that smooth the
428 high-frequency atmospheric forcing. The significant differences mainly occur in the
429 southern YS northwest of Cheju Island and along the YSWC pathway, which suggests
430 that including the high-frequency atmospheric forcing can intensify the saltwater

intrusion into the southern YS. It should also be noted that stronger mean northerly wind stress in Exp-1HR tends to drive fresher water southward from the northern YS, which causes the salinity to be slightly lower in the northern path of the YSWC compared to the two experiments.

A transect along 35°N was chosen to examine the change in vertical structure for the YSWC and related temperature and salinity after including the high-frequency atmospheric forcing (Fig. 9). Notably, the YSWC located between the 50-70 m isobaths is intensified from the upper to lower layers by 1-3 cm/s in EXP-1HR compared to that in EXP-MON. Excluding the high-frequency atmospheric forcing tends to shift the high-temperature core westward toward the Chinese coast (Fig. 9d, e). The stronger southward Korea Coastal Current (Fig. 9a) transports fresher water southward, and the stronger YSWC advects more saline water northward, which causes the salinity to be lower along the Korean coast and high along the YSWC path (Fig. 9i).

Momentum equation terms in the zonal and meridional equation outputs from the model results are also verified along the transect (Fig. 10 and Fig. 11). In the zonal direction in EXP-1HR (Fig. 10), the dominant terms are the barotropic pressure gradient and Coriolis force. However, the horizontal advection, baroclinic pressure gradient, acceleration, and vertical diffusion terms are also important and cannot be ignored. When the high-frequency atmospheric forcing is excluded in EXP-MON, the Coriolis force is reduced, mainly due to the weakened YSWC velocity. Notably, the barotropic pressure gradient around the YSWC pathway is significantly decreased.

The vertical diffusion term is also reduced, which is mainly caused by the weakened surface wind stress. In the meridional direction, all terms except the vertical advection and horizontal diffusion contribute to the momentum balance. The difference in momentum terms between Exp-1HR and Exp-MON is relatively smaller than that in the zonal direction.

# 4. Discussion

## 4.1 Relative contributions of high-frequency wind and other atmospheric fields

Both the wind and other atmospheric variables (air temperature, relative humidity, sea level pressure, longwave and shortwave radiation) influence the sensible and latent heat fluxes, thus affecting the temperature calculation. However, the wind also affects the temperature distribution through current advection. Nonetheless, there is still some question regarding the high-frequency wind and other atmospheric variable relative contributions to the YSWC-related temperature distribution. Therefore, three additional simulations (Exp-WIND-MON, Exp-HEAT-MON, and Exp-WIND-MON-HEAT-SET) were run. The descriptions of the three experiments were shown previously in section 2.3 and Table 1.

Fig. 12 shows the differences in the simulated time-mean temperature between Exp-1HR and the designed experiments (a-c: Exp-1HR minus Exp-MON; d-f: Exp-1HR minus Exp-WIND-MON; g-i: Exp-1HR minus Exp-HEAT-MON; and j-l: Exp-1HR minus Exp-WIND-MON-HEAT-SET). The simulated time-mean temperature is higher in both experiments, excluding the high-frequency variations in all atmospheric variables (Exp-MON, Fig. 12a-c), and only the wind anomalies were

475 filtered in the experiment (Exp-WIND-MON, Fig. 12 d-f). The simulated mean
476 temperature is increased by up to 1°C along the YSWC pathway and 2°C near the
477 coastal region. There is very little difference in the simulation results between
478 Exp-MON and Exp-WIND-MON, except that the magnitude of the temperature
479 increment is slightly smaller for Exp-WIND-MON. If we exclude the high-frequency
480 variations in atmospheric variables but the high-frequency wind anomalies remain
481 (Exp-HEAT-MON, Fig. 12g-i), the simulated mean temperature resembles that of the
482 control run (Exp-1HR) and only increases very slightly (the difference was smaller
483 than 0.5°C in most areas of the YS). Hence, high-frequency perturbations in the wind
484 field have a greater influence on the mean temperature than other atmospheric
485 variables in the YS during winter, since the wind not only drives the ocean current
486 directly but also affects the heat fluxes through the bulk formula.

487 To isolate the direct effect of high-frequency wind forcing on the temperature
488 simulation, we used the monthly average wind forcing and heat flux (including net
489 surface heat flux and shortwave radiation) provided by the control run (Exp-1HR) to
490 drive the model. Therefore, the heat flux in this experiment is the same as that in the
491 control run. The only difference in the model setup is the monthly wind forcing used
492 in this experiment. The difference in the mean temperature (Exp-1HR minus
493 Exp-WIND-MON-HEAT-SET) is shown in Fig. 12j-l. The mean temperature along
494 the YSWC pathway is increased by 0.5-2°C when the high-frequency wind speed is
495 included. It is suggested that stronger wind stress when considering the
496 high-frequency wind speed tends to drive more cold coastal water southward along

497 the eastern YS. As a result, the simulated YSWC is intensified and brings more warm
498 water northward along the western trough of the YS.

499 **4.2 Role of frequent storm bursts on warm and salty water intrusion**

500 Previous studies have revealed that the warm water advected by the Cheju
501 Warm Current (CWC) intrudes intermittently northwestward into the southern YS
502 (Lie et al., 2009, 2013, 2015) during frequent winter storms. A strong winter storm
503 burst forces cold water southward along the coastal region of the YS, and warm water
504 is driven northward by the CWC and YSWC when the storm lessens. Reanalysis
505 atmospheric data from NCEP/CFSv2 show that multiple strong storms occurred in the
506 winter of 2017 (Fig. S1). Although our model experiments shown in section 3 have
507 confirmed that the high-frequency wind forcing tends to enhance the warm and salty
508 water intrusion into the southern YS (Fig. 6-8), we are still unsure how these storms
509 affect the warm salty water transport into the southern YS entrance.

510 Observations of sea level anomalies and subtidal currents presented in section
511 2 suggest that the subtidal sea level fluctuations at coastal stations and subtidal
512 currents are highly correlated under multiple winter storms, especially at mooring
513 station M2, which is located near the southern YS entrance. To reveal the relations
514 between the multiple storm-induced intermittent northward burst of the YSWC and
515 the warm salty water intrusion at the southern YS entrance, we more closely
516 examined the observed current at M2 and sea level fluctuations at both the west and
517 east coasts of the YS. Fig. 13 shows the time series of observed subtidal sea level
518 fluctuations at stations Lvsi and MokPo and the subtidal meridional current

519 component at station M2. The intermittent northwestward intrusion of CWC into the
520 southern YS can also be noted from the observations near the southern YS entrance.
521 The observed subtidal current was not always northward but featured significant
522 synoptic fluctuations, with northward and southward currents occurring alternately
523 (Fig. 13a). The observed subtidal sea level elevations at both the west and east coasts
524 of the YS also fluctuated at a prominent synoptic scale. Notably, the intermittent
525 northward current is closely correlated with the synoptic variations in sea level at both
526 the west and east coasts of the YS.

527 We focused on the period in February in Fig. 13b to more clearly see the
528 relations between subtidal variations in sea level and synoptic current fluctuations.
529 The domain-averaged surface wind indicates several prominent weather processes. A
530 strong northerly storm burst and relaxation can be noted after 12 February. The
531 northerly wind tends to drive water in the BS and northern YS southward. When the
532 wind relaxes, the high sea level signal moves northward along the Korean coast, and
533 the low sea level propagates southward along the coast of China, which causes the sea
534 level anomaly to be out of phase at stations on the west and east coasts of the YS
535 (black and magenta lines in Fig. 13b). The lowpass filtered current at station M2 also
536 shows the quick oscillation of the YSWC under frequent synoptic events. The
537 northward current burst corresponds to low sea level in the western YS and high sea
538 level in the eastern YS. When the sea level pattern is reversed to be high in the east
539 and low in the west, the southern YS entrance is dominated by a southward current.
540 This provides evidence that the synoptic perturbations in the surface wind forcing are

mainly responsible for the short time scale fluctuations of the YSWC.

To understand the dynamic mechanism of the phenomenon described in the above observations, we verified the model results. The model-simulated 6-hourly snapshots of the SSH anomaly and subtidal current at 50 m depth during the observational time period are shown in Fig. 14. Similar to previous modeling studies (Hu et al., 2017; Qu et al., 2017; Ding et al., 2018), the cyclonic rotation of high and low sea levels along the BS and YS coasts during synoptic weather events can be very clearly noted. The subtidal current responds strongly to sea level adjustment. A northward currents dominate the central YS when low sea level occurs west of the YS and high sea level occurs east of the YS. When the sea level is high to the west and low to the east, the current reverses toward south. The model results well represent the synoptic character of the YSWC during winter storms. The episodic strong northward intrusion of the YSWC is highly related to sea level adjustment due to the propagation of coastal trapped waves along the YS shelf (Hu et al., 2016; Ding et al., 2018; Ding et al., 2019; Li and Huang, 2019).

It can be concluded that the high-frequency weather systems associated with frequent winter storm bursts and wind relaxation have the potential to excite trapped coastal waves, which modify the sea level distribution and induce high-frequency synoptic variations in the YSWC. For example, the high sea level moves northward along the Korean coast, and low sea level advances southward along the coast of China during wind relaxation, which increases the westward sea level-related barotropic pressure gradient force. Thus, both the YSWC and westward intrusion of

563 the CWC are intensified, which induces acceleration of the warm salty water intrusion
564 into the southern YS. In contrast, a low sea level propagates northward along the
565 Korean coast, and high sea level moves southward along the Chinese coast, which
566 builds the eastward sea level gradient, and the YSWC is decreased or even reversed
567 toward south. The CWC mainly flows eastward without intruding northwestward. The
568 warm and salty water intrusion is decreased.

569 Previous studies have suggested the importance of winter storm bursts and
570 relaxation, which cause the northwestward intrusion of the CWC to bring warm and
571 salty water into the southern YS in the frontal region (Lie et al., 2009, 2015). As
572 mentioned above, the intermittent intrusion of warm and salty water is closely
573 associated with the high-frequency wind-induced sea level gradient at the southern
574 YS entrance. The dynamics of synoptic variability in the YSWC are determined here
575 based on the model output. We verified the momentum terms from the model outputs
576 at station M2 in the southern YS entrance in both the along-shelf (NW-SE) and
577 cross-shelf (SW-NE) directions.

578 Fig. 15 shows the time series of all momentum terms at M2 during February
579 2017. In the along-shelf direction, the momentum balance can be predominantly
580 determined by four terms, i.e., the acceleration, barotropic pressure gradient, Coriolis
581 force, and vertical diffusion. The other terms are negligibly small and can be ignored.
582 The dominant terms are the barotropic pressure gradient and Coriolis force. The
583 acceleration and vertical diffusion terms cannot be ignored. The sign of the
584 acceleration is in accordance with that of the barotropic pressure gradient, indicating

585 that it is the sea level-related barotropic pressure gradient that mainly drives the
586 acceleration of the flow in the along-shelf direction. In the cross-shelf direction, a
587 geostrophic balance held with the Coriolis force was mainly balanced by the
588 barotropic pressure gradient. The other terms only make minor contributions to this
589 balance and can be ignored. The signs of the dominant momentum terms were
590 occasionally reversed and were in accordance with the synoptic current fluctuations
591 shown in Fig. 13b, which further highlights the important effect of the high-frequency
592 wind-induced sea level gradient on the intermittent intrusion of warm and salty water
593 into the southern YS.

## 594 5. Conclusion

595 In this paper, we evaluate the impact of the high-frequency atmospheric forcing
596 in simulating the YSWC and warm salty water transport in the YS during winter. A
597 control and six sensitivity experiments were performed using an unstructured regional
598 ocean model. The study focused on the period from January to March 2017, which is
599 when direct observations were available. A model-data comparison shows that the
600 simulation results are closer to the observations after including the high-frequency
601 atmospheric forcing. A dramatic response of the YSWC was noted when filtering the
602 high-frequency atmospheric forcing in the BS and YS during winter. The comparison
603 of model experiments with and without atmospheric forcing associated with
604 high-frequency weather systems shows that the high-frequency atmospheric forcing
605 intensifies the magnitude of the time-mean YSWC by 40-100%, lowers the mean
606 temperature by 1°C, and strengthens the mean salinity by 0.2-0.5 psu along the

YSWC pathway. The model results also show that the removal of high-frequency atmospheric phenomena greatly dampens the synoptic variability in the strength of the YSWC. The high-frequency atmospheric forcing is mainly responsible for the episodic fluctuations in the YSWC.

We confirm that the high-frequency variations in wind forcing impact the YSWC and mean temperature far more substantially than other atmospheric variables, such as air temperature, in the YS during winter. The high-frequency wind not only directly drives the ocean current but also affects the heat fluxes through the bulk formula. Both observations and model results indicate that the high-frequency atmospheric forcing associated with a frequent winter storm burst and relaxation has the potential to excite trapped coastal waves propagating cyclonically around the BS and YS coasts, which acts as a very important factor that influences the synoptic variability in the YSWC and intermittent warm and salty water intrusion into the southern YS. For some relatively strong weather events, such as the successive storm bursts during 15-25 February 2017, the 7-day running mean or monthly averaging were very severe, and the wind forcing may no longer be able to excite energetic coastal trapped waves, which may not be favorable for heat and salt transport into the southern YS.

We have presented evidence that “switching on” the synoptic variability in atmospheric forcing is responsible for an increase in the intensity of the regional circulation and heat transport of the YS during winter. Therefore, this study highlights the need for a closer investigation of the impact of high-frequency atmospheric

forcing on the regional circulation in coastal seas. The change in the frequency of winter storms also acts as a very important factor impacting the intensity of the YSWC and warm salty water intrusion. The frequency of storms is usually defined as "storminess" (Munday and Zhai, 2017). Future climate change potentially impacts storminess in the YS during winter, which tends to change the amount of synoptic variability in the atmospheric forcing. Thus, the regional circulation in the YS should be influential. The effect of storminess on the YSWC needs further investigation in the future.

## Appendix A: Model validation

We compare the sea level fluctuations obtained from coastal stations in the BS and YS with the control simulation (Fig. A1). The locations of these costal tide stations are shown in Fig. 1. The sea level fluctuations from the control run show good agreement with those derived from the observations at coastal stations. The strong synoptic variations in sea level at all coastal stations around the BS and YS coasts in the control simulation correspond well with the observations. The mean correlation coefficients between the observations and simulations at the 16 coastal stations all reach 0.92. Both the observed and model-simulated time-distance contours of sea level fluctuations indicate the cyclonic propagation of sea level signals around the BS and YS coasts. Simultaneously, there are also some disagreements between the simulations and observations, as the model seems to overestimate the magnitude of sea level fluctuations during some of the synoptic weather systems. For example,

651 synoptic events occurred during 16-23 January, 12-25 February, and 15-27 March.
652 The differences found in the sea level comparison may originate from an inaccurate
653 surface forcing and bathymetry in coastal seas.

654 The time series of observed sea level anomalies are compared to the model results
655 in Exp-1HR and Exp-7DAY (Fig. A2). The model results in EXP-1HR capture the
656 fluctuations, although they overestimate the amplitude of the sea level anomaly
657 during multiple storm events. It is also clear that the model fails to resolve the
658 synoptic sea level fluctuations in EXP-7DAY when the high-frequency atmospheric
659 forcing is ignored. The quick oscillations of sea level during the storms are filtered
660 out in EXP-7DAY.

661 We also compare the observed subtidal current collected from mooring stations
662 and simulations (Fig. A3). We found that the model does a decent job of capturing the
663 synoptic variability and magnitudes of the subtidal currents at both M1 and M2. The
664 observed characteristics of strong current fluctuations in winter and weak current
665 fluctuations in spring are also represented by the model. Both the observations and
666 model results indicate the strong northward current burst of the YSWC during
667 frequent winter storms, especially in winter. There are also some discrepancies
668 between the simulations and observations. The model results underestimate the
669 magnitudes of both meridional and zonal current components at the two stations
670 before 20 January. The model also overestimates the magnitude of subtidal currents
671 during strong winter storm bursts, especially the meridional current component. For
672 example, from 20-26 January and 15-25 February, the mean observation-model

673 current difference is 2.69 cm/s and 2.10 cm/s for zonal and meridional components at
674 station M1 and is 3.13 cm/s and 3.24 cm/s for that at M2, respectively.

675 The model-simulated time-averaged currents in Exp-1HR and Exp-7DAY are
676 compared with those from the observations (Fig. A4). Including the high-frequency
677 atmospheric forcing in the model (EXP-1HR) enables enhancement of the time-mean
678 current magnitude. Thus, the simulated mean current in EXP-1HR is closer to the
679 observations compared with the model results in EXP-7DAY. Excluding the synoptic
680 atmospheric forcing not only reduced the magnitude of the time-mean current but also
681 changed the current direction. For example, at mooring station M2 (Fig. A4b), the
682 northwestward current was changed to be northeastward in the upper layers when the
683 high-frequency atmospheric forcing was ignored in EXP-7DAY.

684 The temperature and salinity between the simulation and observations from the
685 CTD cruise in the YS in January 2017 were also compared (Fig. A5). As the water is
686 less stratified during winter, we only show the comparison of surface and bottom
687 layers. The model properly represents the observed temperature and salinity
688 distributions. The cold water in coastal areas and relatively warm water in the outer
689 shelf are well represented by the model. Both the observations and model results
690 show the northwestward intrusion of a warm tongue along the western YS trough. The
691 model simulated a relatively higher warm tongue extending northwestward in the
692 western YS compared with the observations. The model-simulated salinity
693 distribution also agrees with the observations with low salinity water near the coastal
694 region and high salinity water from the YSWC in the deeper region. However, the

model-simulated salinity is lower than the observations, especially in shallow water regions, which may be induced by inaccurate estimates of freshwater discharge from the Changjiang River.

The observed and simulated vertical profiles of the average temperature and salinity at all the CTD stations are shown in Fig. A6. Notably, the model-simulated temperature profile in both Exp-1HR and Exp-7DAY agree well with the observations (Fig. A6a). The simulated mean temperature profile is more accurate in EXP-1HR than in EXP-7DAY. Excluding the synoptic atmospheric forcing tends to amplify the temperature difference between the model and observations. The mean difference between the observations and model results decreases from 0.811°C to 0.805°C when considering the high-frequency atmospheric forcing. Notably, the simulated salinity profile differs from the observed structure (Fig. A6b). Including the high-frequency atmospheric forcing cannot improve the simulations, although the discrepancy between the observations and model reduces from 0.569 psu to 0.561 psu.

## Acknowledgments

This work was jointly supported by the National Natural Science Foundation of China (grants 41430963, 41876006, and 41676004) and the National Fund Committee-Shandong joint fund (No. U1706215). Data and samples were collected onboard R/V “Beidou”, implementing the open research cruise NORC2019-01 supported by NSFC Ship time Sharing Project (project number: 41849901). We thank Dr. Ke Chen from the Woods Hole Oceanographic Institution for helping us to improve the manuscript. We thank the Data and Simulation Center of the Physical Oceanography Laboratory, Ocean University of China, for providing supercomputers for all the model simulations. We thank the National Marine Data and Information Service of China, University of Hawaii Sea Level Center, global model of Estimating the Circulation and Climate of the Ocean Phase II, NCEP, OSU Tidal Data Inversion and Bureau of Hydrology, Ministry of Water Resources of P. R. China for providing valuable data. The observational data used in this work are available at Ocean and Atmosphere Data Center of Ocean University of China (coadc.ouc.edu.cn).

## References

724 Chen, C., Liu, H., & Beardsley, R. C. (2003). An unstructured, finite-volume,
725 three-dimensional, primitive equation ocean model: Application to coastal
726 ocean and estuaries. *Journal of Atmospheric and Oceanic Technology*, 20(1),
727 159–186, doi:10.1175/1520-0426.
728 Chen, C. S., Huang, H. S., Beardsley, R. C., Liu, H. D., Xu, Q. C., & Cowles, G.
729 (2007). A finite-volume numerical approach for coastal ocean circulation
730 studies: comparisons with finite difference models. *Journal of Geophysical*
731 *Research*, 112(C03018), 1–34, doi:10.1029/2006JC003485.
732 Chen, D., Liu, W., Zebiak, S., Cane, M., Kushnir, Y., & Witter, D. (1999). Sensitivity
733 of the tropical Pacific Ocean simulation to the temporal and spatial resolution
734 of wind forcing. *Journal of Geophysical Research-Oceans*, 104, C5,
735 11,261-11,271.
736 Ding, Y., Bao, X., Yao, Z., Song, D., Song, J., Gao, J., & Li, J. (2018). Effect of
737 coastal trapped waves on the synoptic variations of the Yellow Sea Warm
738 Current during winter. *Continental Shelf Research*, 167, 14-31.
739 Ding, Y., Bao, X., Yao, Z., Bi, C., Wan, K., Bao, M., Jiang, Z., Song, J., & Gao, J.
740 (2019). Observational and model studies of synoptic current fluctuations in the
741 Bohai Strait on the Chinese continental shelf. *Ocean Dynamics*, 69:323-351.
742 Duteil, O. (2019). Wind synoptic activity increases oxygen levels in the tropical
743 Pacific Ocean. *Geophysical Research Letters*, 46.
744 https://doi.org/10.1029/2018GL081041.
745 Egbert, G., & Erofeeva, S. (2002). Efficient inverse modeling of barotropic ocean

746 tides. *Journal of Atmospheric and Oceanic Technology*. 19, 22,475-22,502.
747 Esbensen, S. K., & Reynolds, R. W. (1981). Estimating monthly averaged air-sea
748 transfers of heat and momentum using the bulk aerodynamic method. *Journal*
749 *of Physical Oceanography*, 11, 457–465, doi:10.1175/1520
750 0485(1981)011,0457:EMAAST.2.0.CO;2.
751 Fairall, C. W., Bradley, E. F., Rogers, D. P., Edson, J. B., & Young, G. S. (1996). Bulk
752 parameterization of air-sea fluxes for Tropical ocean-global atmosphere
753 coupled–ocean atmosphere response experiment. *Journal of Geophysical*
754 *Research*, 101(C2), 3747-3764, doi:10.1029/95JC03205.
755 Gulev, S. K. (1994). Influence of space–time averaging on the ocean–atmosphere
756 exchange estimates in the North Atlantic midlatitudes. *Journal of Physical*
757 *Oceanography*, 24, 1236–1255, doi:10.1175/
758 1520-0485(1994)024,1236:IOSTAO.2.0.CO;2.
759 Hu, Z., Wang, D., He, X., L, M., Wei, J., Pan, D., & Bai, Y. (2017). Episodic surface
760 intrusions in the Yellow Sea during relaxation of northerly winds. *Journal of*
761 *Geophysical Research*, 122, 6533–6546, doi:10.1002/2017JC012830.
762 Hsueh, Y., & Romea, R. D. (1983). Wintertime Winds and Coastal Sea-Level
763 Fluctuations in the Northeast China Sea. Part I: Observations. *Journal of*
764 *Physical Oceanography*, 13(11), 2091-2106, doi: doi:10.1175/1520-
765 0485(1983)013<2091:WWACSL>2.0.CO;2.
766 Hsueh, Y. (1988). Recent observations in the eastern Yellow Sea. *Journal of*
767 *Geophysical Research*, 93: 6875-6884.

768 Holdsworth, A., & Myers, P. (2015). The influence of high-frequency atmospheric
769 forcing on the circulation and deep convection of the Labrador Sea. *Journal of*
770 *Climate*, 28:4980-4996.
771 Large, W. G., & Pond, S. (1981). Open ocean momentum fluxes in moderate to strong
772 winds. *Journal of Physical Oceanography*, 11:324–336
773 Lie, H. (1999). On the Huanghai (Yellow) Sea circulation: A review by current
774 measurements. *Acta Oceanologica Sinica*, 18(3): 355-374.
775 Lie, H. J., Cho, C. H., & Lee, S. (2009). Tongue-shaped frontal structure and warm
776 water intrusion in the southern Yellow Sea in winter. *Journal of Geophysical*
777 *Research*, 114, C01003. https:// doi.org/10.1029/2007JC004683.
778 Lie, H. J., Cho, C. H., & Lee, S. (2013). Frontal circulation and westward transversal
779 current at the Yellow Sea entrance in winter. *Journal of Geophysical Research-*
780 *Oceans*, 118, 3851–3870. https://doi.org/10.1002/jgrc.20280.
781 Lie, H. J., Cho, C. H., & Jung, K. T. (2015). Occurrence of large temperature
782 inversion in the thermohaline frontal zone at the Yellow Sea entrance in winter
783 and its relation to advection. *Journal of Geophysical Research-Oceans*, 120,
784 417–435. https://doi.org/10.1002/2014JC010653.
785 Lie, H. J., Cho, & C. H. (2016). Seasonal circulation patterns of the Yellow and East
786 China Seas derived from satellite-tracked drifter trajectories and hydrographic
787 observations. *Progress of Oceanography*, 146, 121–141.
788 Lin, X., Yang, J., Guo, J., Zhang, Z., Yin, Y., Song, X., & Zhang, X. (2011). An
789 asymmetric upwind flow, Yellow Sea Warm Current: 1. New observations in

790 the western Yellow Sea. *Journal of Geophysical Research*, 116, C04026.
791 https://doi.org/10.1029/2010JC006513.
792 Liu, X., Chiang, K. P., Liu, S. M., Wei, H., Zhao, Y., & Huang, B. Q. (2015).
793 Influence of the Yellow Sea warm current on phytoplankton community in the
794 central Yellow Sea. *Deep Sea Research-Part I*, 106, 17–29.
795 Ma, J., Qiao, F., Xia, C., & Kim, C. (2006). Effect of the Yellow Sea Warm Current on
796 the winter temperature distribution in a numerical model. *Journal of*
797 *Geophysical Research*, 111, C11S04:1-12.
798 Moon, J. H., Hirose, N., & Yoon, J. H. (2009). Comparison of wind and tidal
799 contributions to seasonal circulation of the Yellow Sea. *Journal of Geophysical*
800 *Research*, 114, C08016. https://doi.org/10.1029/2009JC005314.
801 Munday, D. R., & Zhai, X. (2017). The impact of atmospheric storminess on the
802 sensitivity of the Southern Ocean circulation to wind stress changes. *Ocean*
803 *Modelling*, 115:14-26.
804 Pang, I. C., Moon, J. H., Lee, J. H., Hong, J. S., & Pang, S. J. (2017). Modeling
805 temperature inversion in southeastern Yellow Sea during winter 2016. *Journal*
806 *of Geophysical Research-Oceans*, 122, doi:10.1002/2017JC012718.
807 Qu, L., Lin, X., Hetland, R., & Guo, J. (2017). The asymmetric continental shelf wave
808 in response to the synoptic wind burst in a semi-enclosed double-shelf basin.
809 *Journal of Geophysical Research-Oceans*, 123, 131-148.
810 https://doi.org/10.1002/2017JC013025
811 Shi, Y., Gao, J. H., Sheng, H., Du, J., Jia, J. J., Wang, Y. P., Li, J., & Bai, F. L. (2019).

812 Cross-front sediment transport induced by quick oscillation of the Yellow Sea
813 Warm Current: Evidence from the sedimentary record. *Geophysical Research*
814 *Letters*, 46. https://doi.org/ 10.1029/2018GL080751.
815 Su, J., Wu, H., Zhang, Y., Liu, Q., & Bai, S. (2005). A coupled ice-ocean model for
816 the Bohai Sea: part II. Case study. *Acta Oceanologica Sinica*, 24, 54–67.
817 Takahashi, S., Isoda, Y., & Yanagi, T. (1995). A numerical study on the formation and
818 variation of a clockwise-circulation during winter in the Yellow Sea. *Journal of*
819 *Oceanography*, 51, 83–98. https://doi.org/10.1007/BF02235938.
820 US Naval Oceanographic Office and the US Naval Ocean Research and Development
821 Activity, 1983. DBDB5 (Digital Bathymetric Data Base-5 Minute Grid). US
822 N.O.O., Bay St. Louis, p 329.
823 Wang, F., Liu, C., & Meng, Q. (2012). Effect of the Yellow Sea Warm Current fronts
824 on the westward shift of the Yellow Sea Warm tongue in winter. *Continental*
825 *Shelf Research*, 45:98-107.
826 Wu, Y., Zhai, X., & Wang, Z. (2016). Impact of synoptic atmospheric forcing on the
827 mean ocean circulation. *Journal of Climate*, 29:5709-5724.
828 Yin, L., Qiao, F., & Zheng, Q. (2014). Coastal-trapped waves in the East China Sea
829 observed by a mooring array in winter 2006. *Journal of Physical Oceanography*,
830 44(2), 576-590, http://dx.doi.org/10.1175/JPO-D-13-07.1.
831 Yu, F., Zhang, Z., Diao, X., & Guo, J. (2010). The observation evidence of the Yellow
832 Sea Warm Current. *Journal of Oceanology and Limnology*, 28, 677–683.
833 https://doi.org/10.1007/s00343-010-0006-2.

834 Zhai, X. (2013). On the wind mechanical forcing of the ocean general circulation,
835 *Journal of Geophysical Research-Oceans*, 118, 6561-6577,
836 doi:10:1002/2013JC009086.
837 Zhai, X., Johnson, H. L., Marshall, D. P., & Wunsch, C. (2012). On the wind power
838 input to the ocean general circulation. *Journal of Physical Oceanography*, 42,
839 1357-1365, doi: 10.1175/JPO-D-12-09.1.
840 Zhou, S., Zhai, X., & Renfrew, I. A. (2018). The impact of high-frequency weather
841 systems on SST and surface mixed layer in the central Arabian Sea. *Journal of*
842 *Geophysical Research-Oceans*, 123, 1091-1104.
843 https://doi.org/10.1002/2017JC013609.

**Figure 1**. Map of the studied region including the Bohai Sea, Yellow Sea and East China Sea. Blue dashed lines denote open boundaries for the regional ocean model. Gray lines show the bathymetry of 10, 50, 70, 200, 1000 and 2000 m. Blue triangle indicates mooring station deployed along the 70 m isobath in the southern Yellow Sea. Red dots denote coastal tide gauge stations along the Bohai Sea and Yellow Sea coast (1: MokPo, 2: YeongKwang, 3: KunSan, 4: InCheon; 5: Donggang, 6: Xiaochangshan, 7: Laohutan, 8: Bayuquan, 9: Qinhuangdao, 10: Tanggu, 11: Longkou, 12: Yantai, 13: Chengshantou, 14: Rizhao, 15: Lianyungang, 16: Lvsi). Black dots denote the CTD stations during winter cruise of 2017. Red dashed line denotes a transect along 35°N crossing the southern Yellow Sea.

**Figure 2**. Time series of sea level anomaly at coastal stations around the Bohai and Yellow Sea coast (a). The sea level fluctuations were shifted downward by 0.8 m to show the sea level variations at each station more clearly. Time-distance contour of sea level anomaly at the 16 coastal stations around the Bohai and Yellow Sea coast is shown in (b). Black dashed line is used to separate the whole observational period into two different time periods. An enlarged view for time-distance contour of sea level anomaly focusing on February is shown in (c).

**Figure 3**. Observed time series of zonal and meridional components of sub-tidal currents at stations M1 and M2 in the southern Yellow Sea during winter and early spring 2017. The currents were lowpass filtered to remove the tidal signals.

**Figure 4**. Temporal average of surface wind stress calculated from hourly CFSv2 winds in Exp-

1HR, with its magnitude in colors and direction by arrows (a). The differences of wind stress magnitude between Exp-1HR and experiment are drawn for (b) Exp-1HR minus Exp-7DAY and (c) Exp-1HR minus Exp-MON. Comparison of time series of wind stress averaged over the southern Yellow Sea among the three experiments is shown in (d) and (e). Black line denotes zonal and meridional wind stress components in Exp-1HR. Red line denotes Exp-7DAY and Blue line denotes Exp-MON.

**Figure 5**. Time-mean net surface heat flux in Exp-1HR (a). Differences of net surface heat flux between Exp-1HR and the other experiments (Exp-1HR minus Exp-7DAY, Exp-1HR minus Exp-MON, Exp-1HR minus Exp-WIND-MON, EXP-HEAT-MON) are shown in (b) – (e). Comparison of time series of net surface heat flux averaged over the southern Yellow Sea is shown in (f). Black line denotes Exp-1HR; Red line denotes Exp-7DAY; Blue line denotes Exp-MON; Cyan line denotes Exp-WIND-MON; Magenta lines denotes Exp-HEAT-MON.

**Figure 6**. Comparison of mean current between Exp-1HR and Exp-MON at 5 m (a), 30 m (c), and 50 m (e). Black arrows denote Exp-1HR and red arrows denote Exp-MON. The differences of current magnitude between Exp-1HR and Exp-MON (Exp-1HR minus Exp-MON) are shown (b), (d) and (f).

**Figure 7**. The mean temperature in Exp-1HR (a, d and g), and Exp-MON (b, e, and h) at 5 m, 30 m and 50 m. The differences of temperature between Exp-1HR and Exp-MON (Exp-1HR minus Exp-MON) are shown in (c), (f), and (i).

**Figure 8**. Same as Figure. 7, but for salinity.

**Figure 9.** Comparison of mean meridional current component, temperature and salinity along the transect at 35°N between Exp-1HR (a, d and g) and Exp-MON (b, e and h). The differences (Exp-1HR minus Exp-MON) are shown in c, f and i.

**Figure 10.** Mean momentum terms in the zonal direction along the transect at 35°N for Exp-1HR and Exp-MON. The differences (Exp-1HR minus Exp-MON) are also shown in this figure. HADV: horizontal advection, VADV: vertical advection, BAROC_P: baroclinic pressure gradient, BAROT_P: barotropic pressure gradient, CORI: Coriolis force, DUDT: acceleration, HDIFF: horizontal diffusion, VDIFF: vertical diffusion.

**Figure 11.** Same as Figure 10, but for the meridional direction.

**Figure 12**. Differences of mean temperature at 5 m, 30 m, and 50 m between Exp-1HR and experiments. (a)-(c): Exp-1HR minus Exp-MON, (d)-(f): Exp-1HR minus Exp-WIND-MON, (g)-(i): Exp-1HR minus Exp-HEAT-MON, (j)-(l): Exp-1HR minus Exp-WIND-MON-HEAT-SET.

**Figure 13**. (a) Time series of observed meridional component of sub-tidal currents at station M2 during winter and early spring 2017. The time series of sea level anomaly at station Lvsi on west coast and MokPo on east coast of YS are also shown in this figure. Black dashed lines denote time

period from 31 January to 28 February. (b) The sub-tidal current component and sea level anomaly from 31 January to 28 February. The domain averaged surface wind from CFSv2/NCEP is also shown in gray sticks.

**Figure 14**. Six hourly snapshot of sea surface height anomaly and sub-tidal current at 50 m depth during several synoptic weather systems from 17 to 23 February. The thick black arrows indicate domain averaged surface wind.

**Figure 15**. Time series of momentum terms in the along shelf (NW-SE) direction and cross shelf (SW-NE) direction. Positive values indicate NW and SW directions.

**Figure A1**. Comparison of low-pass filtered sea level fluctuations at all 16 stations between the observations (a) and control run (b).

**Figure A2**. Time series of low-pass filtered sea level fluctuations from the observations (blue), EXP-1HR (red) and EXP-7DAY (black).

**Figure A3**. Comparison of low-pass filtered current between the observations and model results at station M1 and M2.

**Figure A4**. The time-averaged current at station M1 and M2 from the observations, EXP-1HR and EXP-7DAY.

89 **Figure A5**. Comparison of surface and bottom salinity between the observations and model results
90 from control run. The black dots denote CTD stations. The blue triangles denote the two current
91 mooring stations.
92
93 **Figure A6**. The mean temperature (a) and salinity (b) profile averaged over all the CTD stations
94 from the observations (blue), EXP-1HR (red) and EXP-7DAY (black).
95
96 **Figure S1**. Time series of the hourly atmospheric variables of surface wind (a), air temperature (b),
97 and sea level pressure (c) averaged over the southern Yellow Sea. The atmospheric data are obtained
98 from CFSv2/NCEP.
99
100 **Figure S2**. Comparison of mean current between Exp-1HR and Exp-7DAY at 5 m (a), 30 m (c), and
101 50 m (e). Black arrows denote Exp-1HR and red arrows denote Exp-7DAY. The differences of
102 current magnitude between Exp-1HR and Exp-7DAY (Exp-1HR minus Exp-7DAY) are shown (b),
103 (d) and (f).
104
105 **Figure S3**. The mean temperature in Exp-1HR (a, d and g), and Exp-7DAY (b, e, and h) at 5 m, 30
106 m and 50 m. The differences of temperature between Exp-1HR and Exp-7DAY (Exp-1HR minus
107 Exp-7DAY) are shown in (c), (f), and (i).
108
109 **Figure S4**. Same as Figure. S3, but for salinity.
110

**Figure1.**

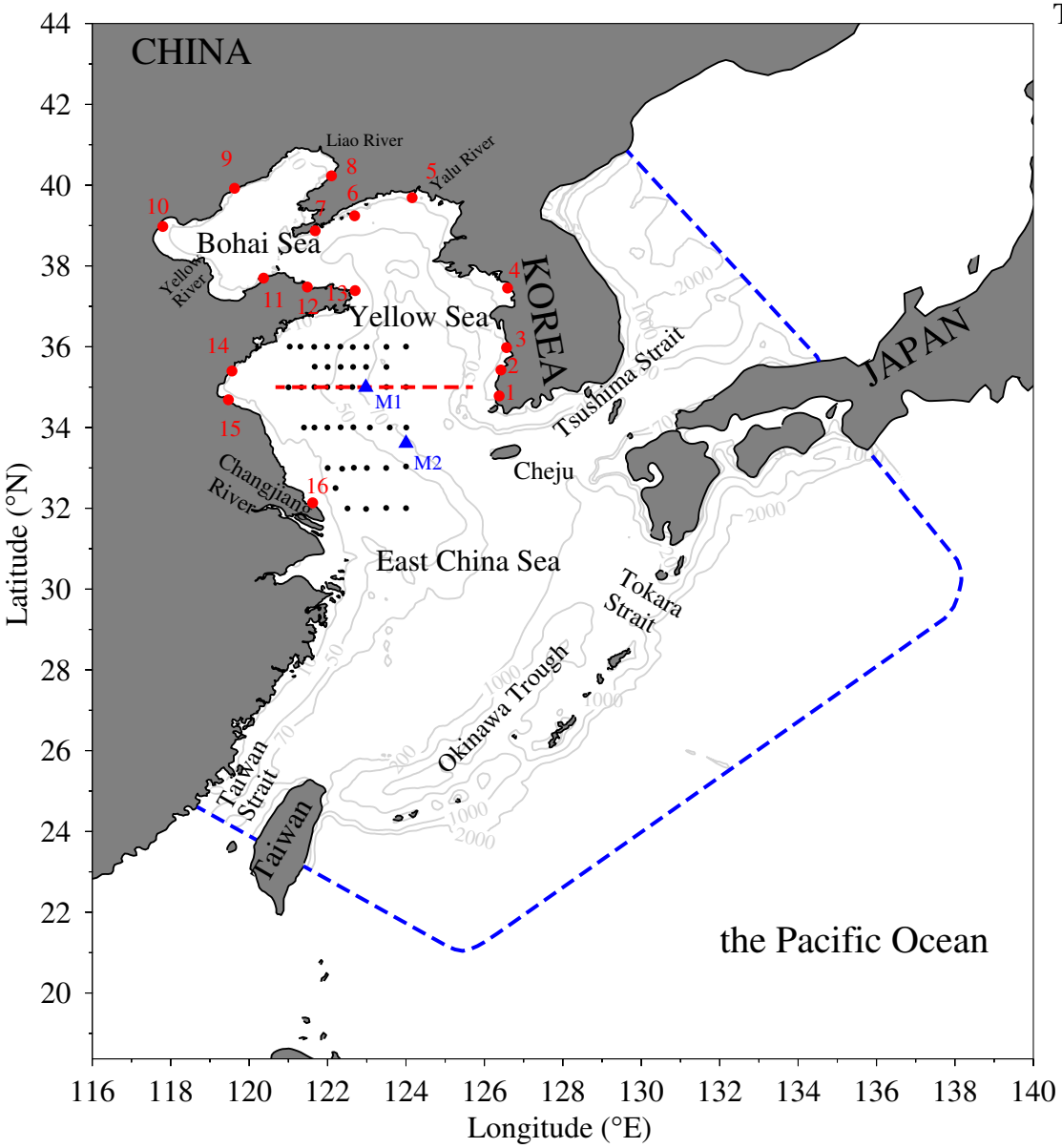


Tidal stations

1: MokPo
2: YeongKwang
3: KunSan
4: InCheon
5: Donggang
6: Xiaochangshan
7: Laohutan
8: Bayuquan
9: Qinhuangdao
10: Tanggu
11: Longkou
12: Yantai
13: Chengshantou
14: Rizhao
15: Lianyungang
16: Lvsi

**Figure2.**

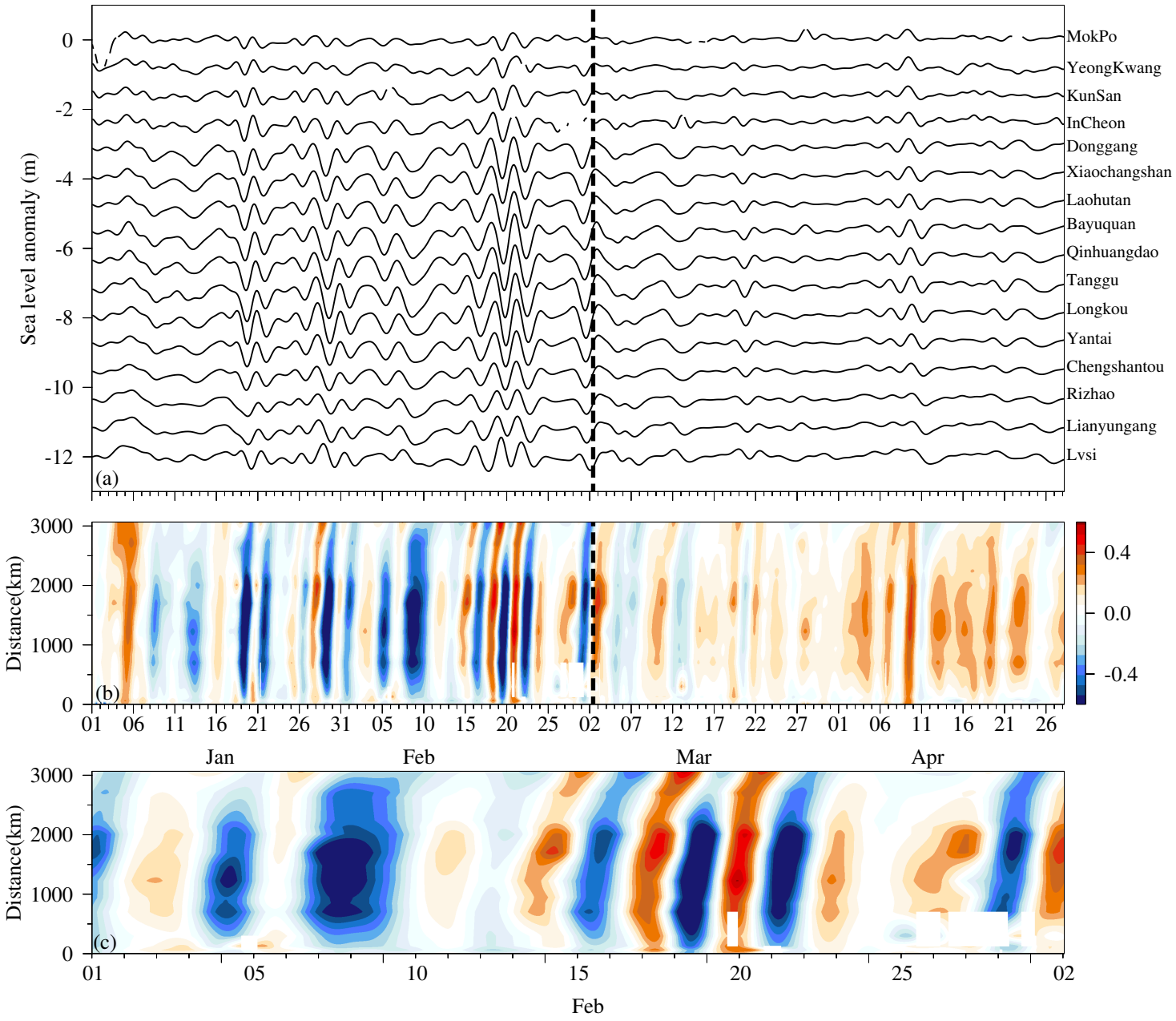
Sea level anomaly (m)
0
-2
-4
-6
-8
-10
-12
(a)
MokPo
YeongKwang
KunSan
InCheon
Donggang
Xiaochangshan
Laohutan
Bayuquan
Qinhuangdao
Tanggu
Longkou
Yantai
Chengshantou
Rizhao
Lianyungang
Lvsi
Distance(km)
3000
2000
1000
0
(b)
0.4
0.0
-0.4
01 06 11 16 21 26 31 05 10 15 20 25 02 07 12 17 22 27 01 06 11 16 21 26
Jan
Feb
Mar
Apr
Distance(km)
3000
2000
1000
0
(c)
01 05 10 15 20 25 02
Feb

**Figure3.**

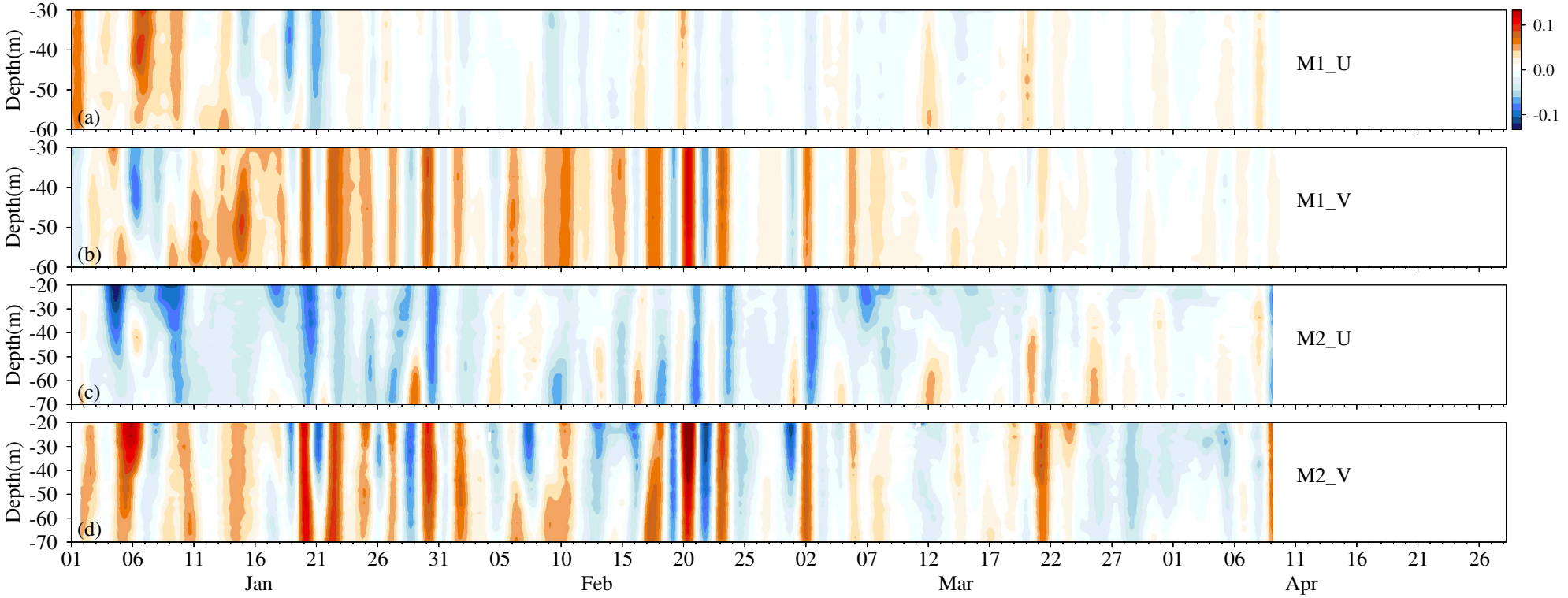
Depth(m)
-30
-40
-50
-60
(a)
M1_U
0.1
0.0
-0.1
(b)
M1_V
-20
-70
(c)
M2_U
(d)
M2_V
01
06
11
16
21
26
31
05
10
15
20
25
02
07
12
17
22
27
Jan
Feb
Mar
Apr

**Figure4.**

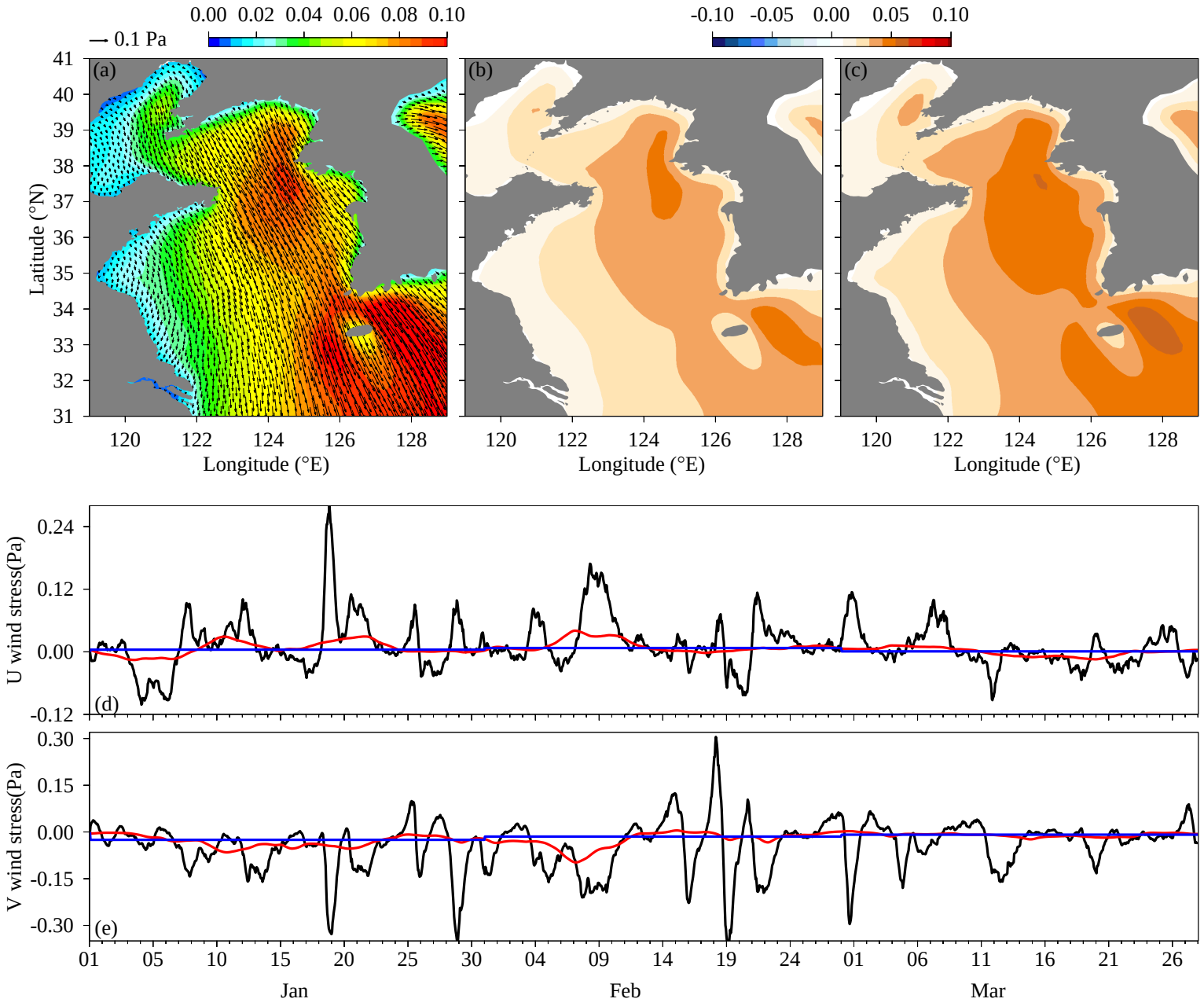
0.00 0.02 0.04 0.06 0.08 0.10
0.1 Pa
-0.10 -0.05 0.00 0.05 0.10
(a)
(b)
(c)
Latitude (°N)
Longitude (°E)
Longitude (°E)
Longitude (°E)


U wind stress(Pa)
V wind stress(Pa)
(d)
(e)
Jan
Feb
Mar

**Figure5.**

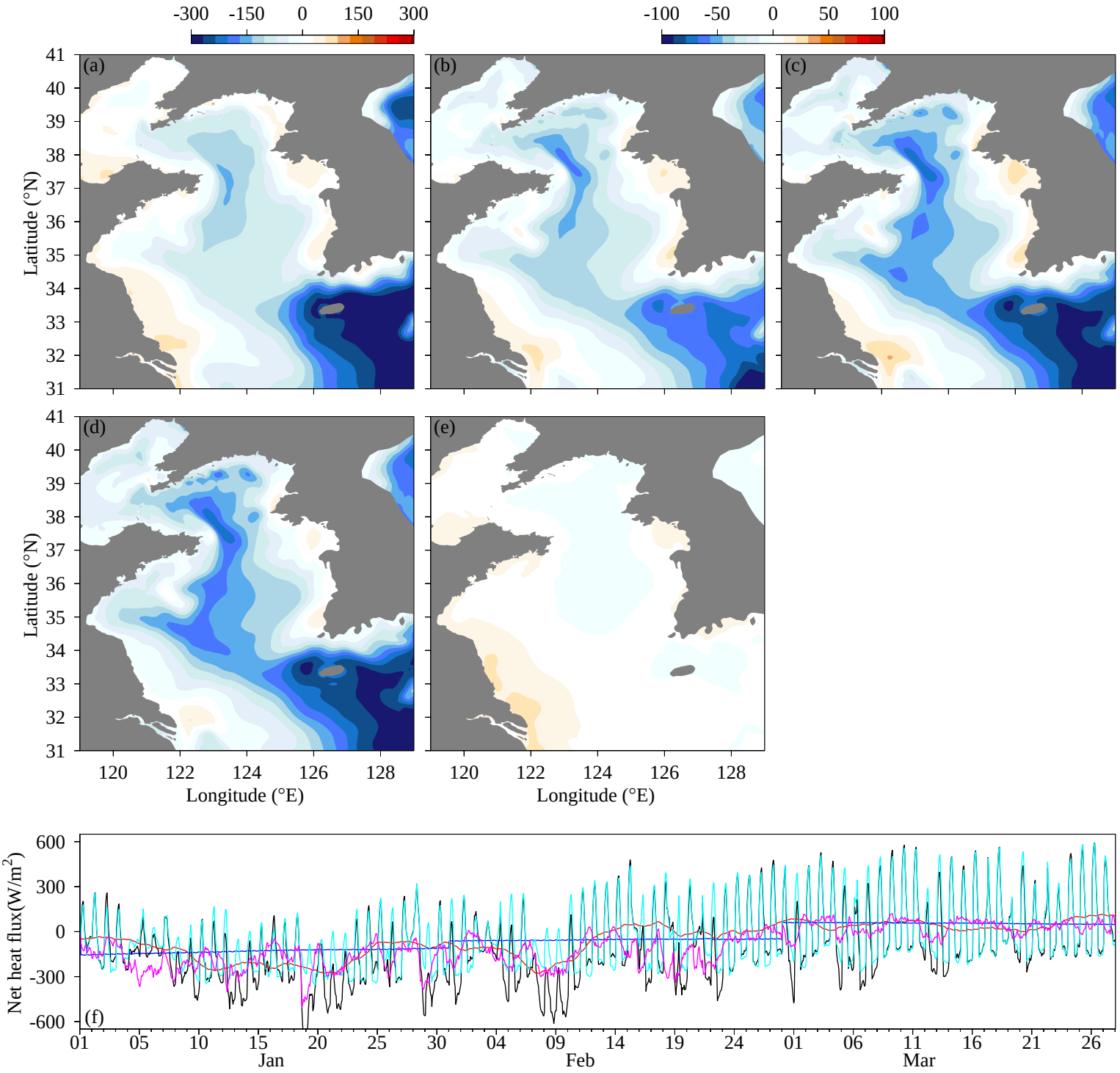
-300 -150 0 150 300
-100 -50 0 50 100
(a)
(b)
(c)
(d)
(e)
Latitude (°N)
Longitude (°E)
41 40 39 38 37 36 35 34 33 32 31
120 122 124 126 128


Net heat flux(W/m2)
600 300 0 -300 -600
(f)
01 05 10 15 20 25 30 04 09 14 19 24 01 06 11 16 21 26
Jan
Feb
Mar

**Figure6.**

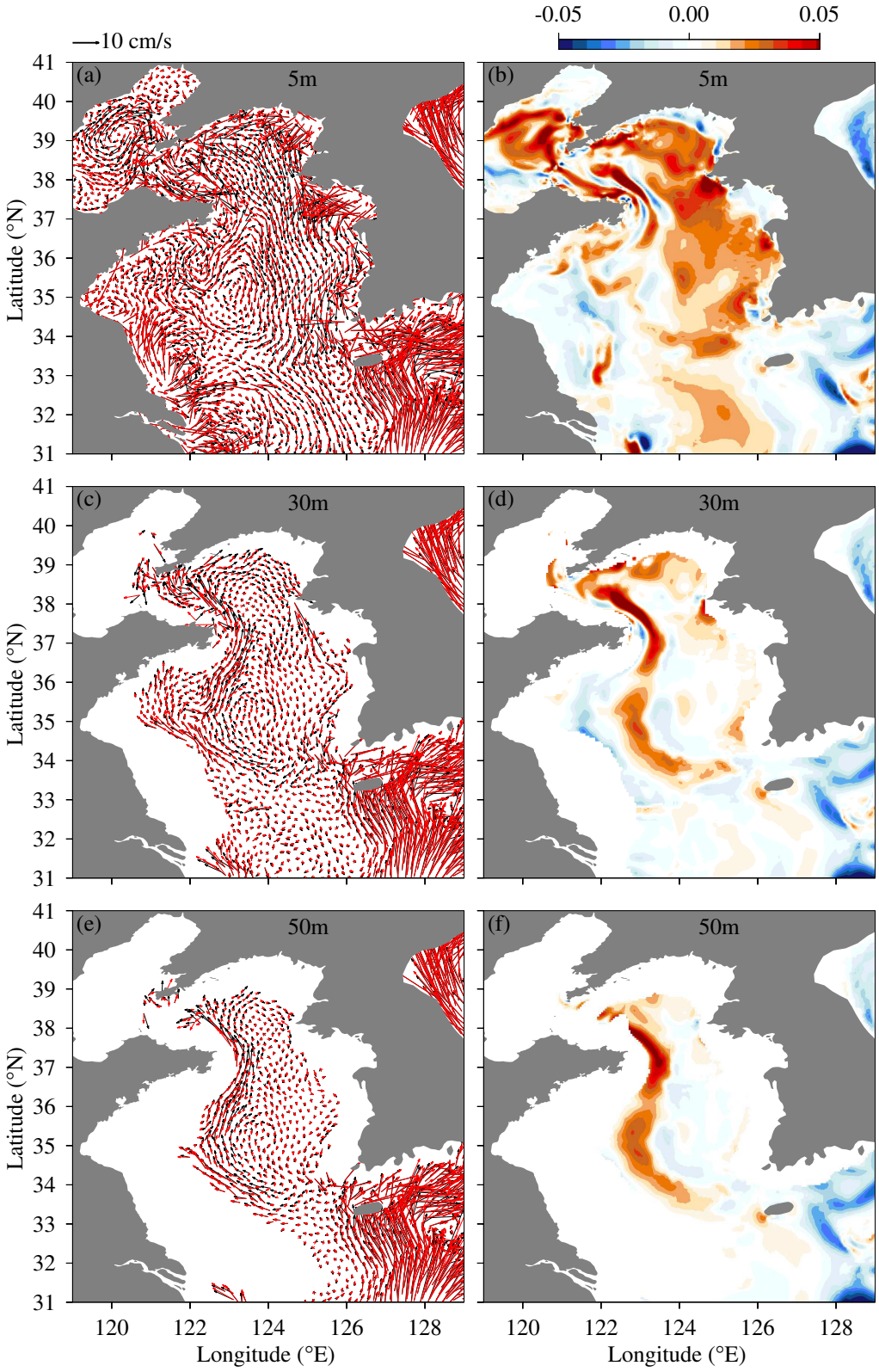
10 cm/s
-0.05
0.00
0.05
(a)
5m
(b)
5m
(c)
30m
(d)
30m
(e)
50m
(f)
50m
Latitude (°N)
Longitude (°E)
41
40
39
38
37
36
35
34
33
32
31
120
122
124
126
128

**Figure7.**

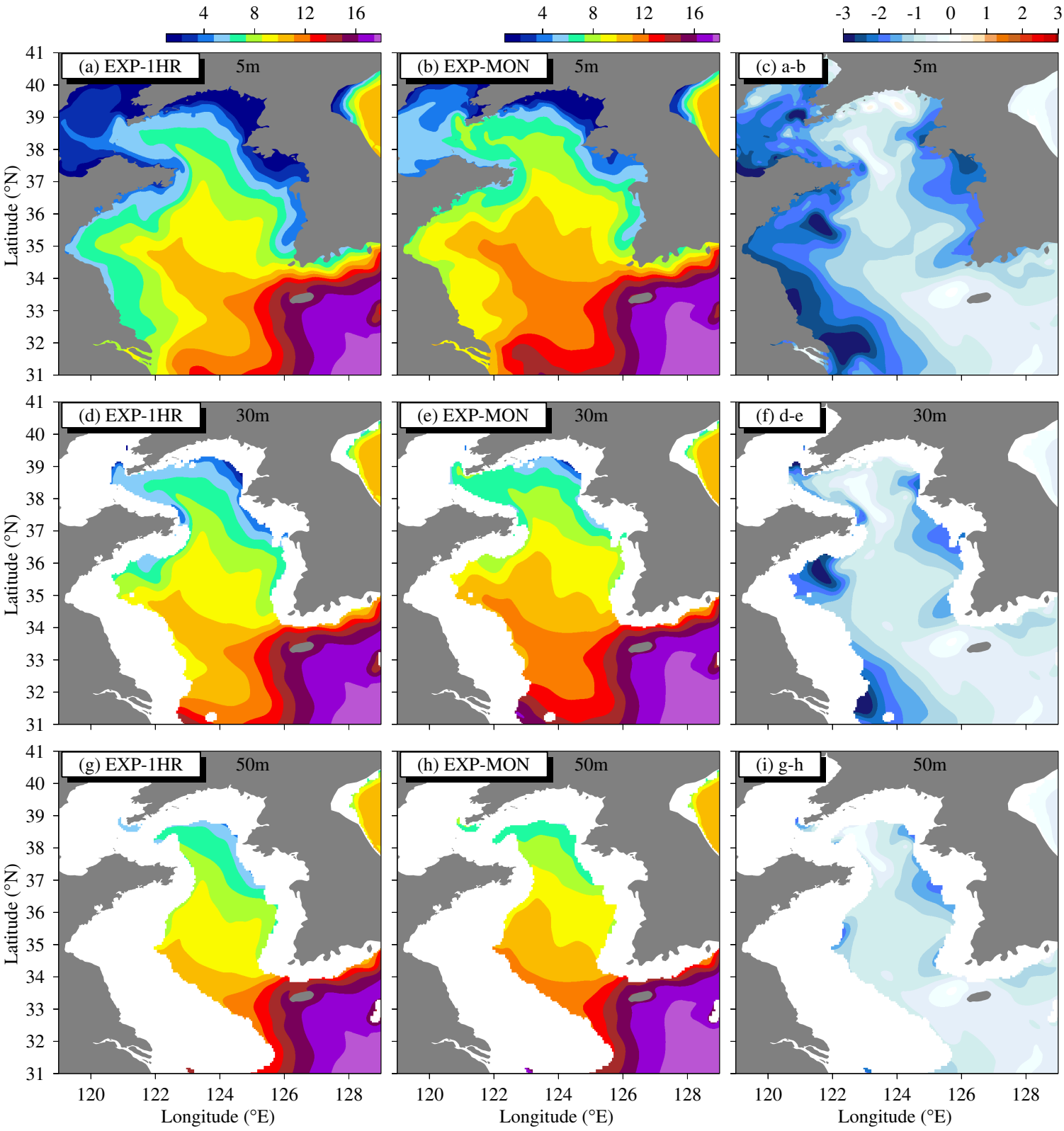
4 8 12 16
4 8 12 16
-3 -2 -1 0 1 2 3
(a) EXP-1HR 5m
(b) EXP-MON 5m
(c) a-b 5m
(d) EXP-1HR 30m
(e) EXP-MON 30m
(f) d-e 30m
(g) EXP-1HR 50m
(h) EXP-MON 50m
(i) g-h 50m
Latitude (°N)
Longitude (°E)
41 40 39 38 37 36 35 34 33 32 31
120 122 124 126 128

**Figure8.**

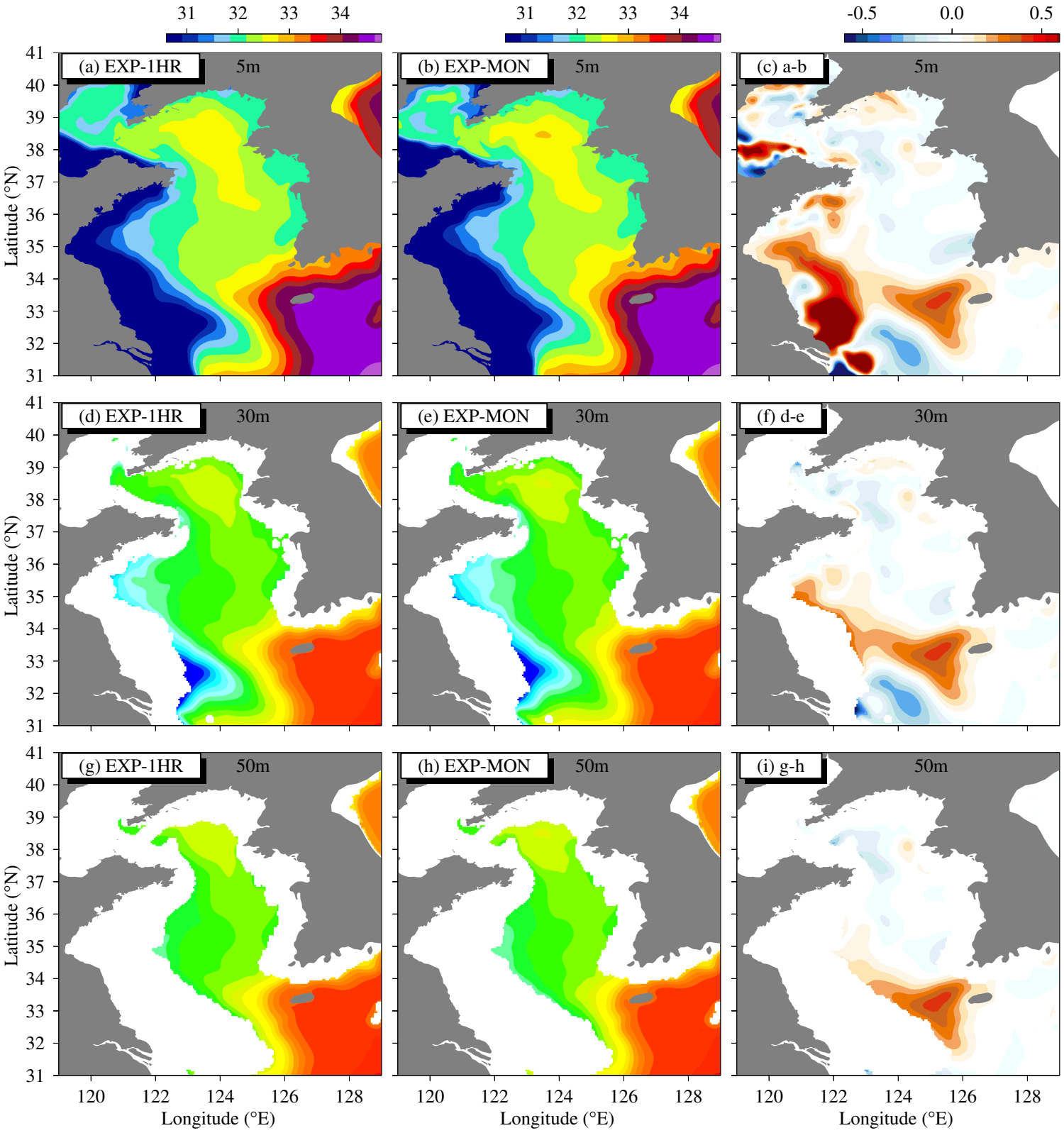
31 32 33 34
31 32 33 34
-0.5 0.0 0.5
(a) EXP-1HR 5m
(b) EXP-MON 5m
(c) a-b 5m
(d) EXP-1HR 30m
(e) EXP-MON 30m
(f) d-e 30m
(g) EXP-1HR 50m
(h) EXP-MON 50m
(i) g-h 50m
Latitude (°N)
Longitude (°E)
41 40 39 38 37 36 35 34 33 32 31
120 122 124 126 128

**Figure9.**

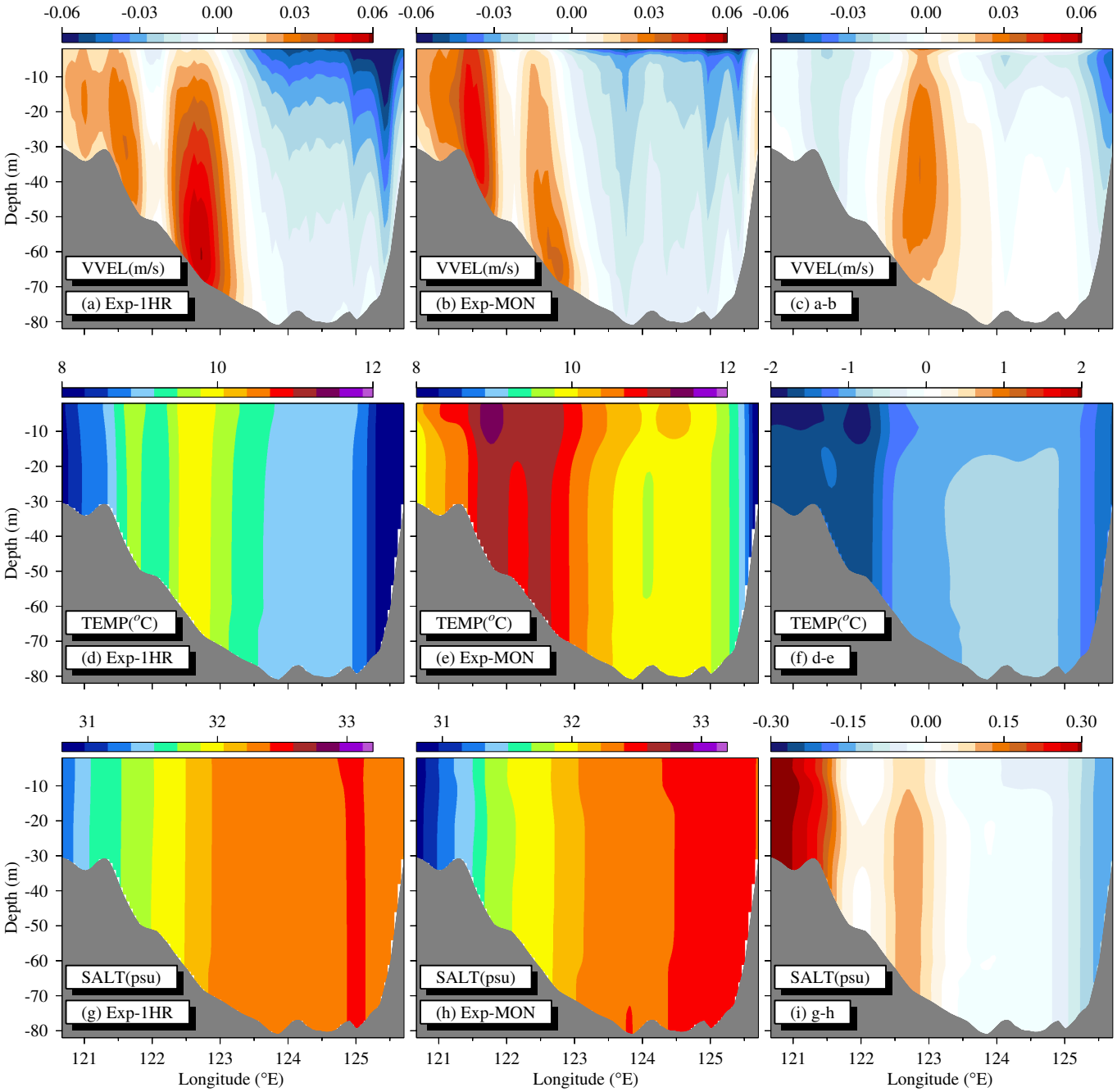
-0.06 -0.03 0.00 0.03 0.06
-0.06 -0.03 0.00 0.03 0.06
-0.06 -0.03 0.00 0.03 0.06
Depth (m)
-10 -20 -30 -40 -50 -60 -70 -80
VVEL(m/s)
(a) Exp-1HR
VVEL(m/s)
(b) Exp-MON
VVEL(m/s)
(c) a-b
8 10 12
8 10 12
-2 -1 0 1 2
TEMP(°C)
(d) Exp-1HR
TEMP(°C)
(e) Exp-MON
TEMP(°C)
(f) d-e
31 32 33
31 32 33
-0.30 -0.15 0.00 0.15 0.30
SALT(psu)
(g) Exp-1HR
SALT(psu)
(h) Exp-MON
SALT(psu)
(i) g-h
121 122 123 124 125
Longitude (°E)
121 122 123 124 125
Longitude (°E)
121 122 123 124 125
Longitude (°E)

**Figure10.**

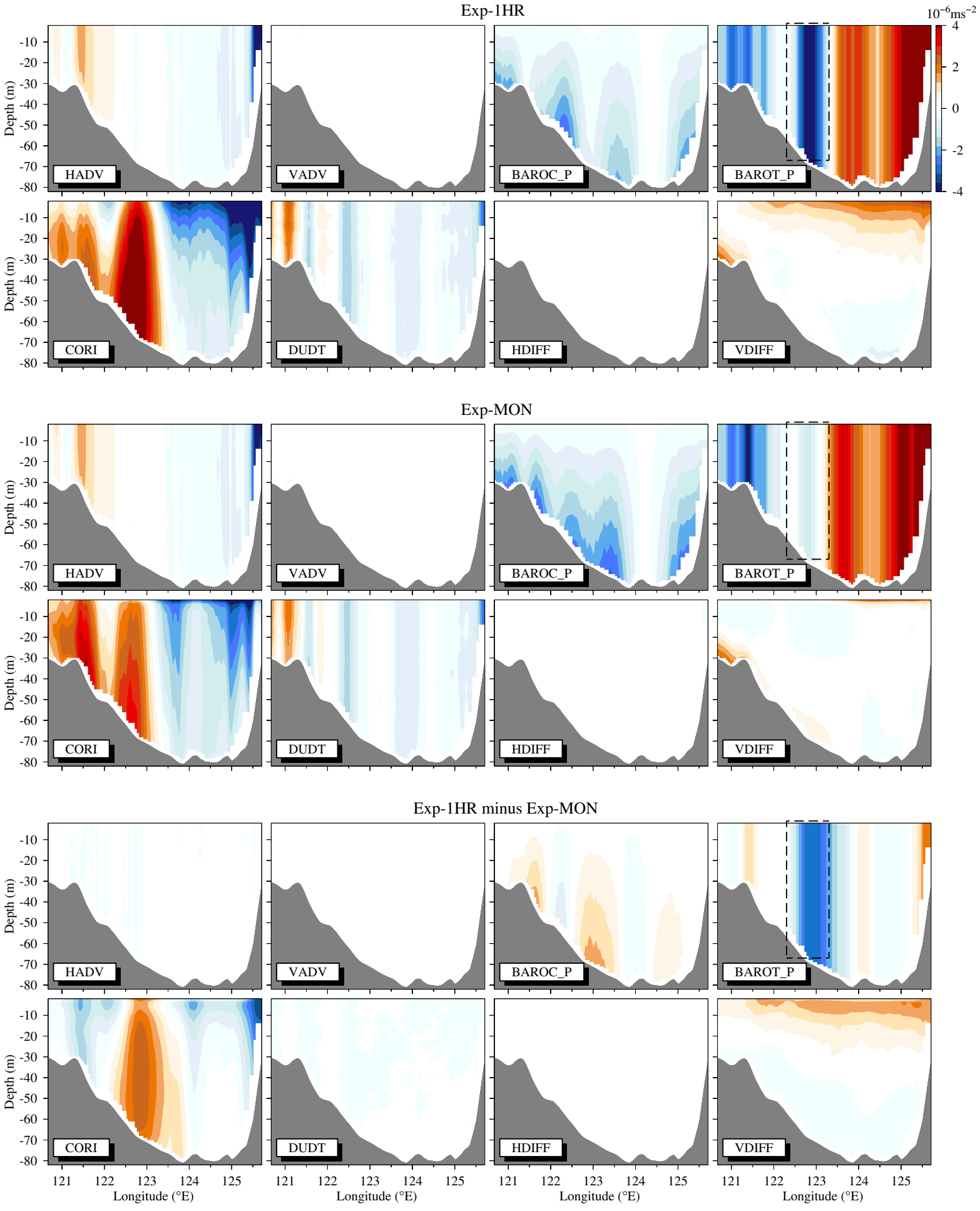
Exp-1HR
$10^{-6}$ms$^{-2}$
4
2
0
-2
-4
Depth (m)
-10
-20
-30
-40
-50
-60
-70
-80
HADV
VADV
BAROC_P
BAROT_P
CORI
DUDT
HDIFF
VDIFF
Exp-MON
Exp-1HR minus Exp-MON
121
122
123
124
125
Longitude (°E)

**Figure11.**

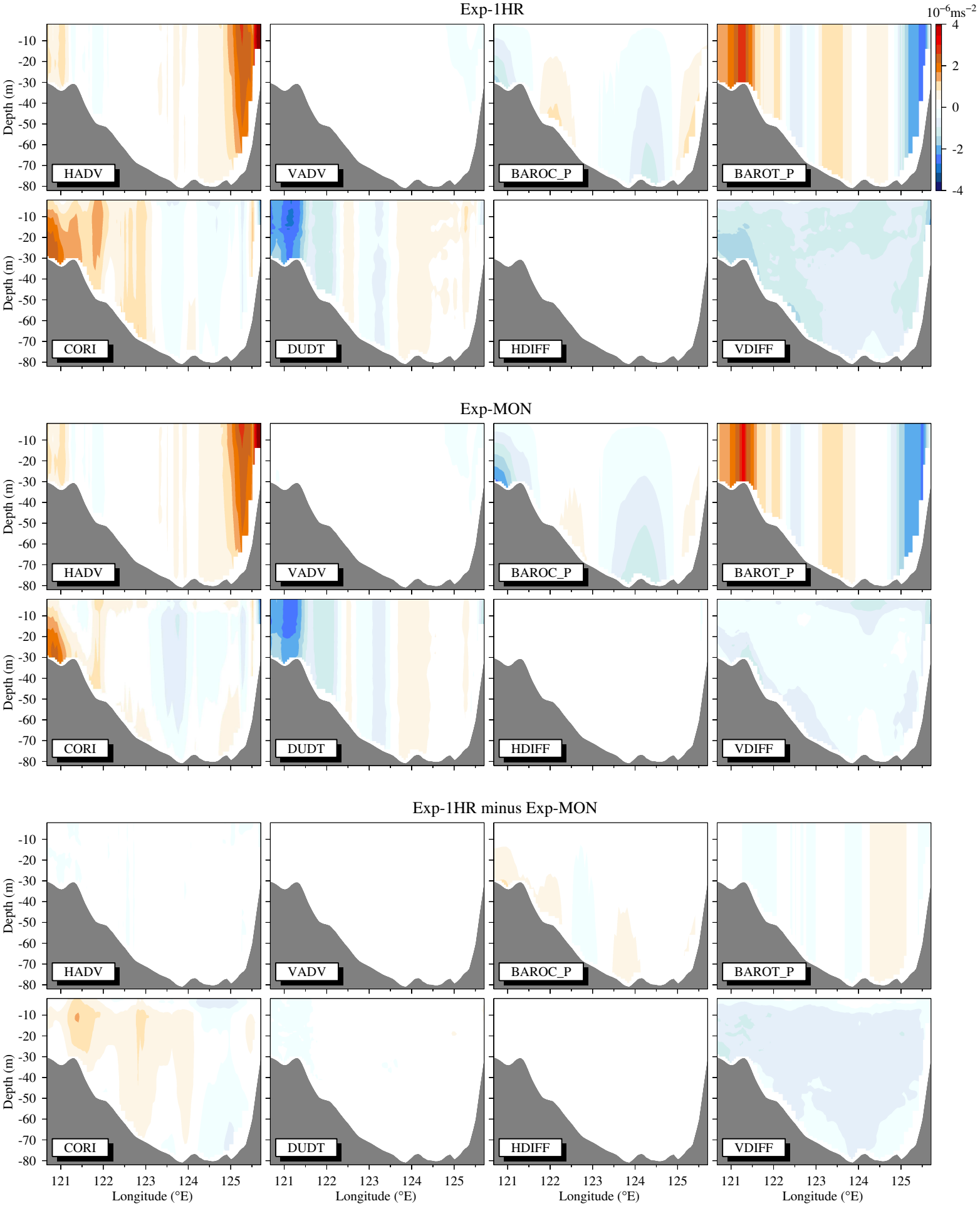
Exp-1HR
$10^{-6}$ms$^{-2}$
4
2
0
-2
-4
Depth (m)
-10
-20
-30
-40
-50
-60
-70
-80
HADV
VADV
BAROC_P
BAROT_P
CORI
DUDT
HDIFF
VDIFF
Exp-MON
Exp-1HR minus Exp-MON
121
122
123
124
125
Longitude (°E)

**Figure12.**

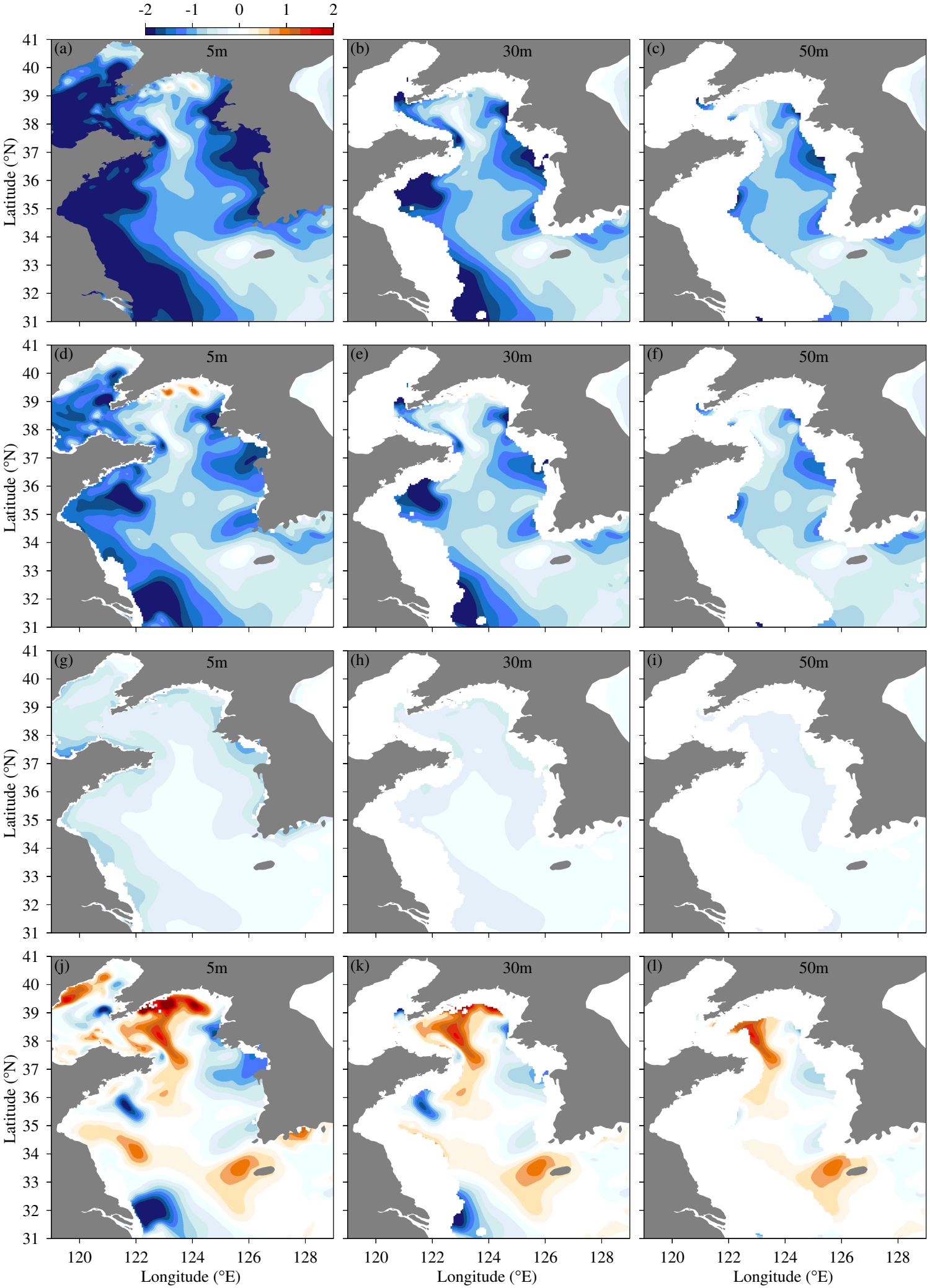
-2
-1
0
1
2
(a)
5m
(b)
30m
(c)
50m
(d)
5m
(e)
30m
(f)
50m
(g)
5m
(h)
30m
(i)
50m
(j)
5m
(k)
30m
(l)
50m
Latitude (°N)
41
40
39
38
37
36
35
34
33
32
31
120
122
124
126
128
Longitude (°E)

**Figure13.**

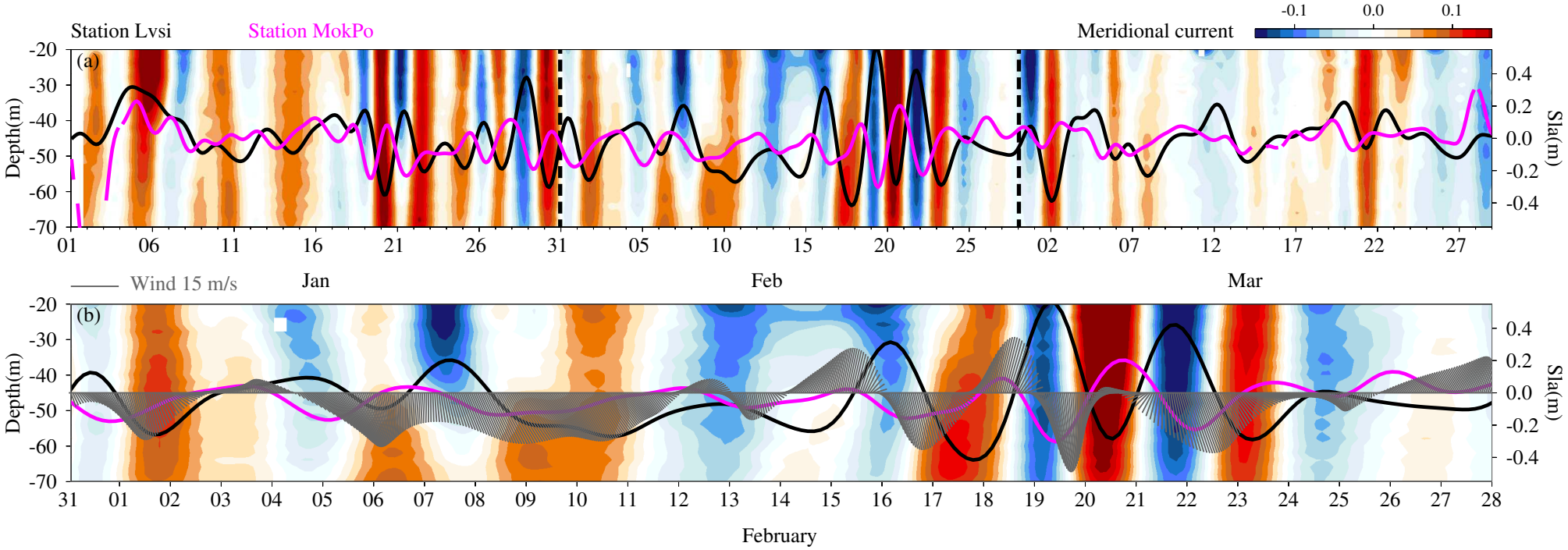
Station Lvsi
Station MokPo
Meridional current
-0.1
0.0
0.1
(a)
Depth(m)
-20
-30
-40
-50
-60
-70
Sla(m)
0.4
0.2
0.0
-0.2
-0.4
01
06
11
16
21
26
31
05
10
15
20
25
02
07
12
17
22
27
Jan
Feb
Mar
Wind 15 m/s
(b)
31
01
02
03
04
05
06
07
08
09
10
11
12
13
14
15
16
17
18
19
20
21
22
23
24
25
26
27
28
February

**Figure14.**

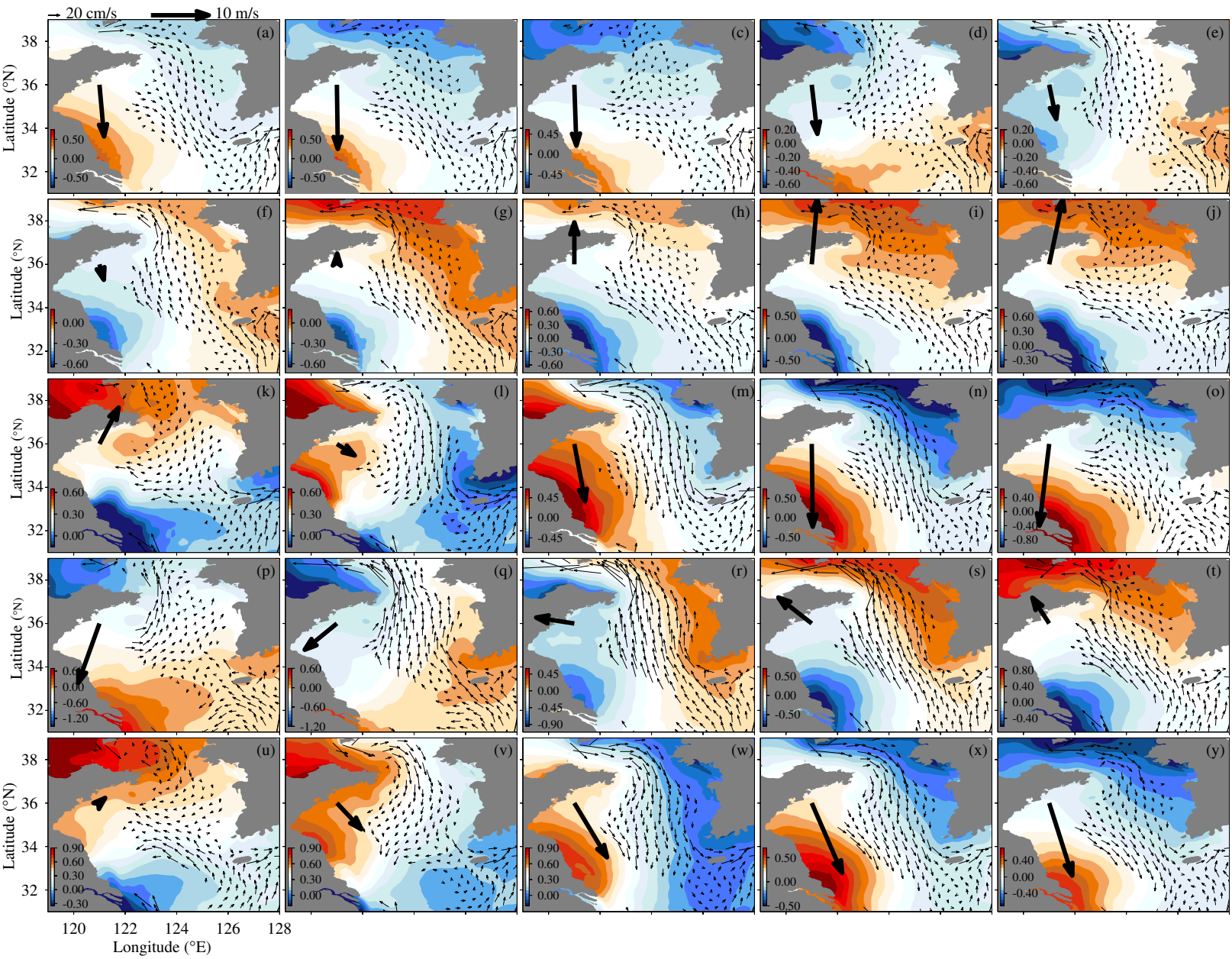
20 cm/s
10 m/s
(a)
(b)
(c)
(d)
(e)
(f)
(g)
(h)
(i)
(j)
(k)
(l)
(m)
(n)
(o)
(p)
(q)
(r)
(s)
(t)
(u)
(v)
(w)
(x)
(y)
Latitude (°N)
Longitude (°E)
120
122
124
126
128
32
34
36
38

**Figure15.**

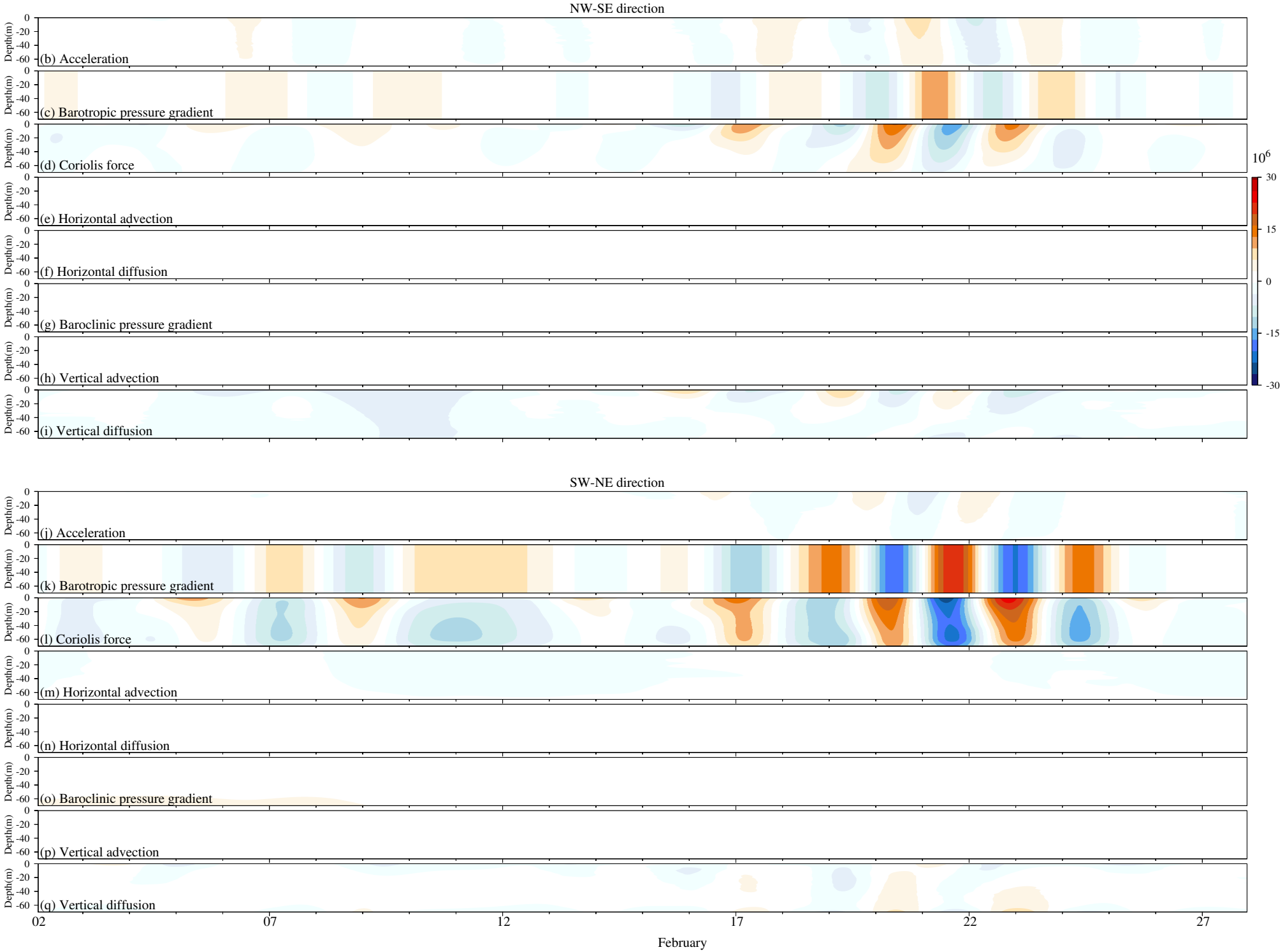
NW-SE direction
(b) Acceleration
(c) Barotropic pressure gradient
(d) Coriolis force
(e) Horizontal advection
(f) Horizontal diffusion
(g) Baroclinic pressure gradient
(h) Vertical advection
(i) Vertical diffusion
SW-NE direction
(j) Acceleration
(k) Barotropic pressure gradient
(l) Coriolis force
(m) Horizontal advection
(n) Horizontal diffusion
(o) Baroclinic pressure gradient
(p) Vertical advection
(q) Vertical diffusion
Depth(m)
0
-20
-40
-60
$10^6$
30
15
0
-15
-30
02
07
12
17
22
27
February

**Figure A1.**

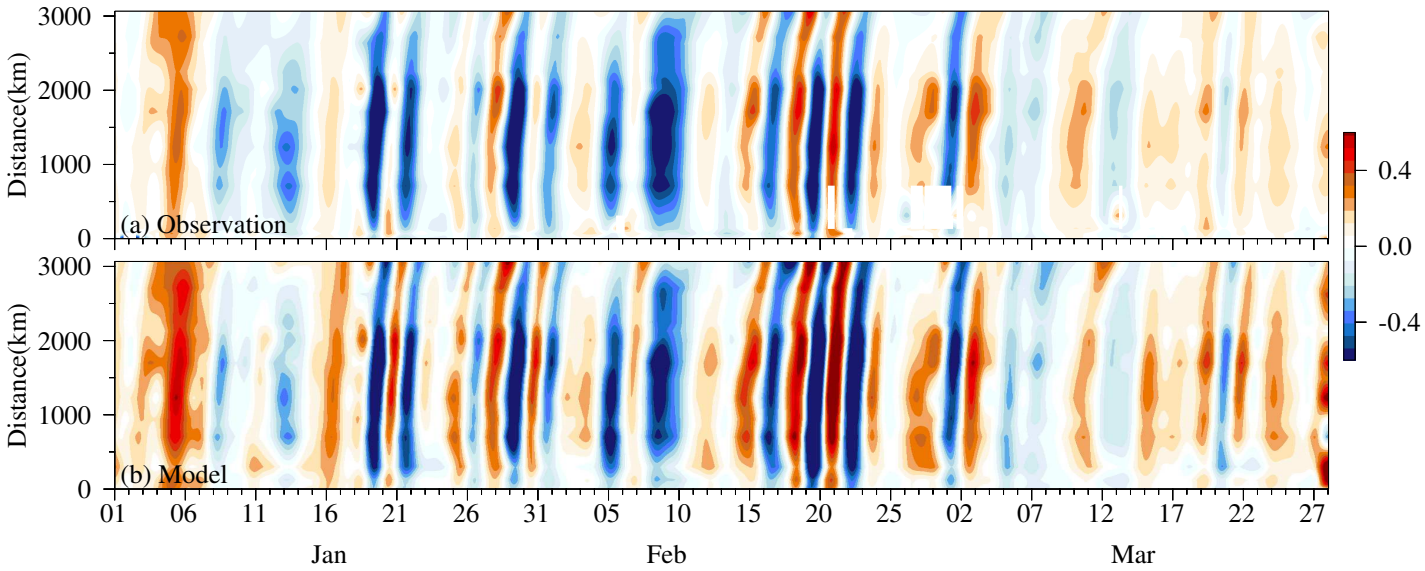
3000
2000
1000
0
Distance(km)
(a) Observation
(b) Model
0.4
0.0
-0.4
01
06
11
16
21
26
31
05
10
15
20
25
02
07
12
17
22
27
Jan
Feb
Mar

**Figure A2.**

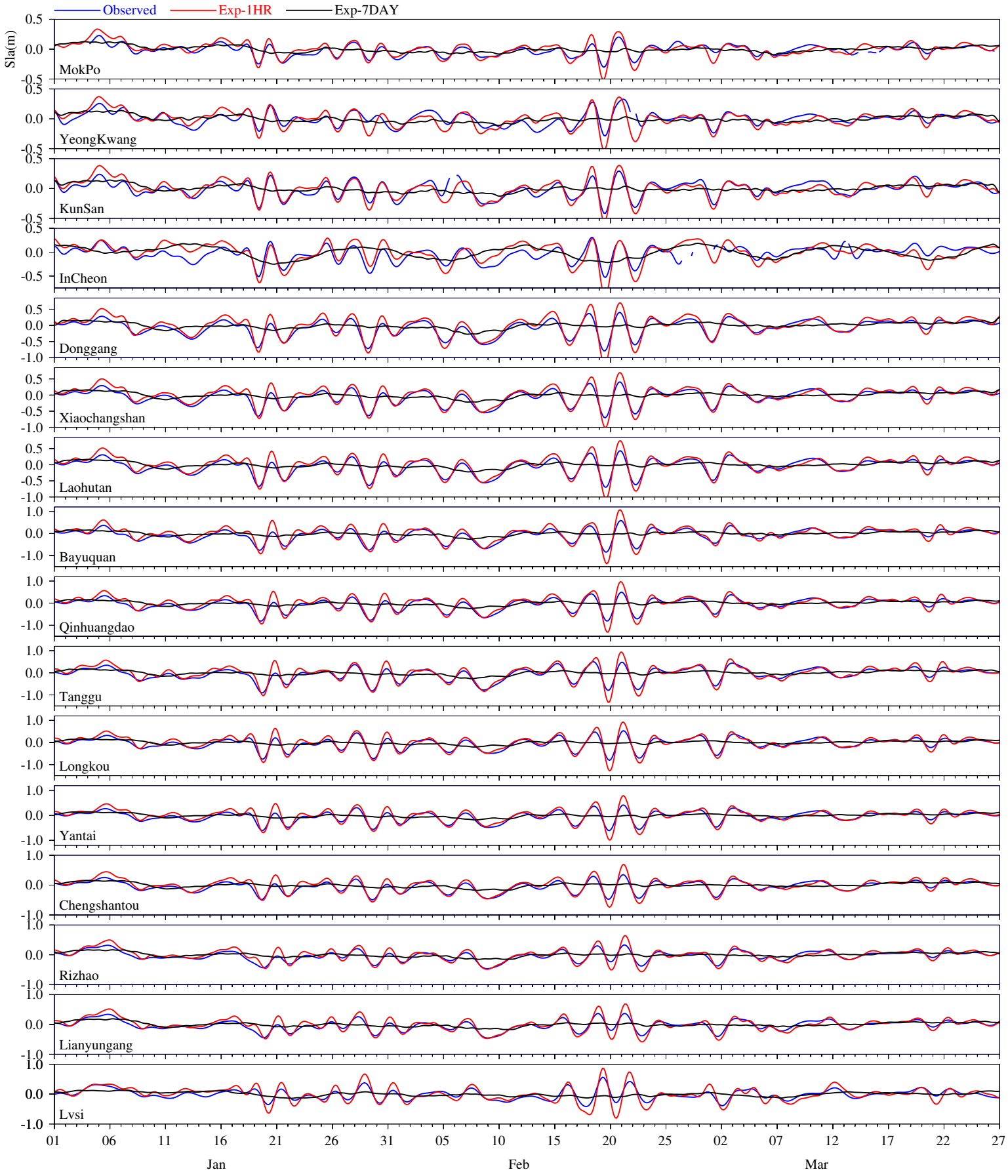
Observed
Exp-1HR
Exp-7DAY
Sla(m)
MokPo
YeongKwang
KunSan
InCheon
Donggang
Xiaochangshan
Laohutan
Bayuquan
Qinhuangdao
Tanggu
Longkou
Yantai
Chengshantou
Rizhao
Lianyungang
Lvsi
01
06
11
16
21
26
31
05
10
15
20
25
02
07
12
17
22
27
Jan
Feb
Mar

**Figure A3.**

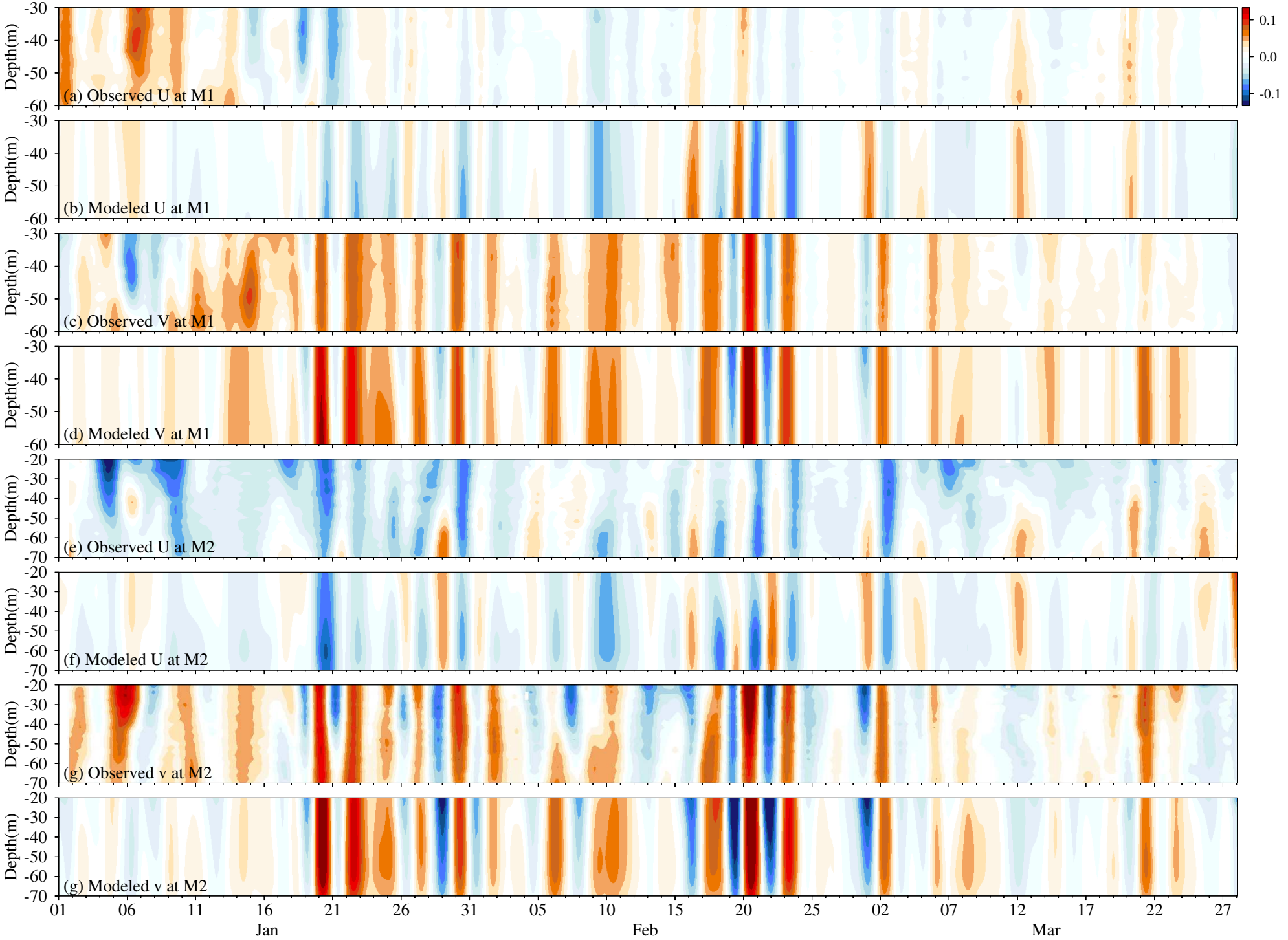
(a) Observed U at M1
(b) Modeled U at M1
(c) Observed V at M1
(d) Modeled V at M1
(e) Observed U at M2
(f) Modeled U at M2
(g) Observed v at M2
(g) Modeled v at M2
Depth(m)
0.1
0.0
-0.1
01 06 11 16 21 26 31 05 10 15 20 25 02 07 12 17 22 27
Jan
Feb
Mar

**Figure A4.**

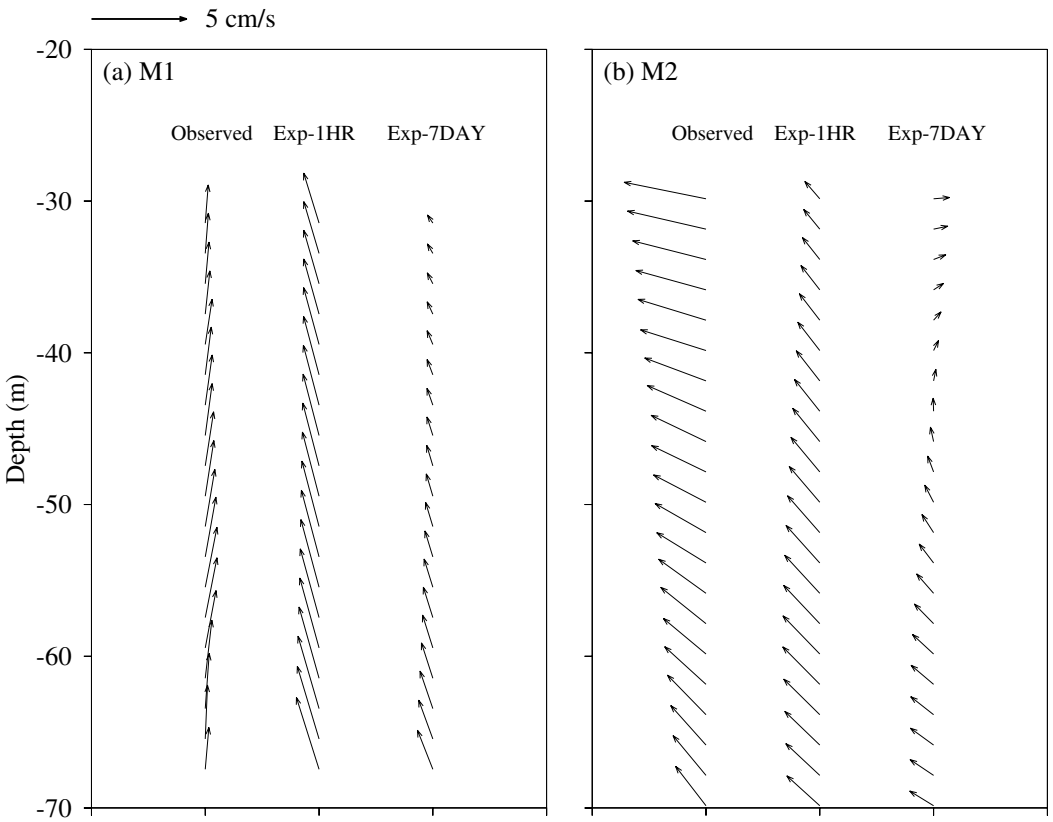
5 cm/s
-20
-30
-40
-50
-60
-70
Depth (m)
(a) M1
Observed
Exp-1HR
Exp-7DAY
(b) M2
Observed
Exp-1HR
Exp-7DAY

**Figure A5.**

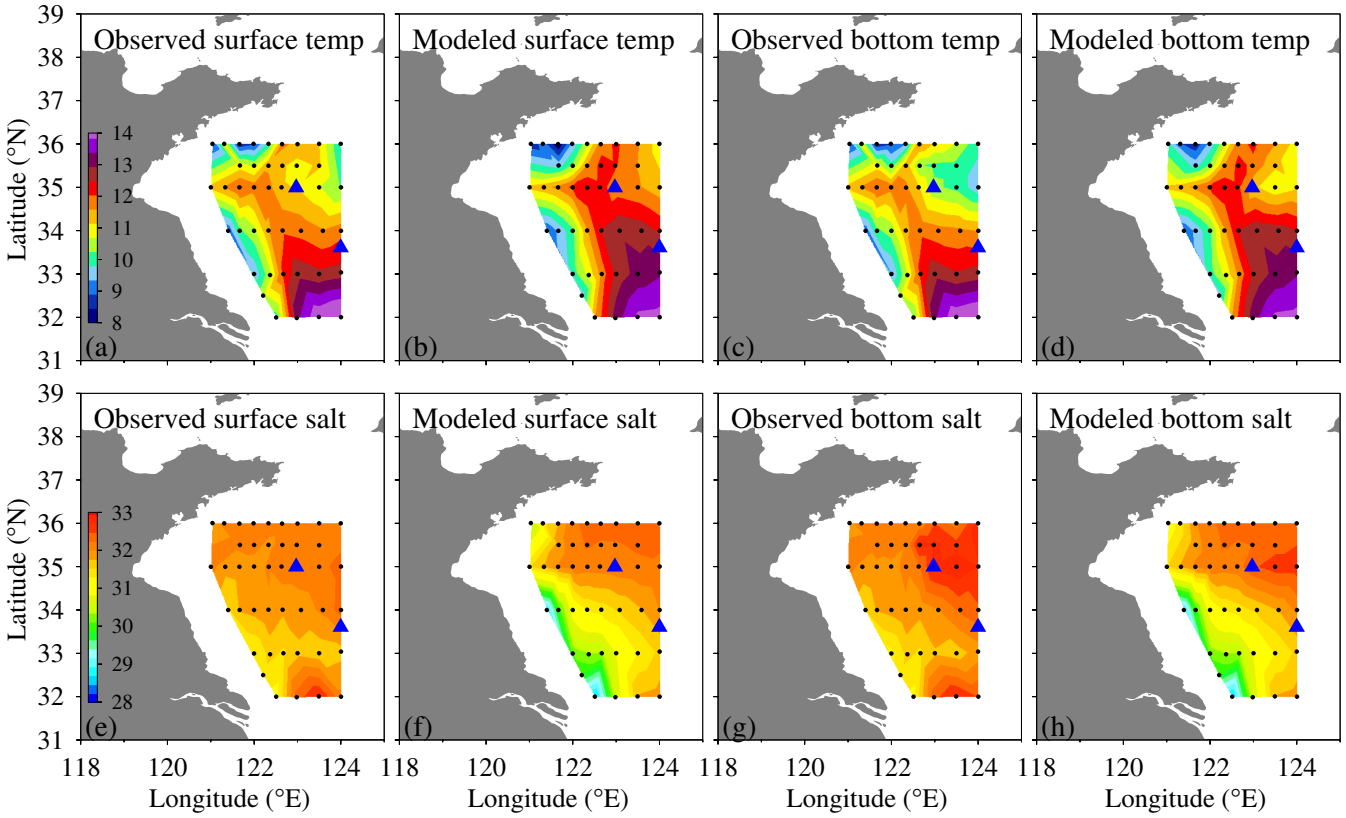
Observed surface temp
Modeled surface temp
Observed bottom temp
Modeled bottom temp
Observed surface salt
Modeled surface salt
Observed bottom salt
Modeled bottom salt
(a)
(b)
(c)
(d)
(e)
(f)
(g)
(h)
14
13
12
11
10
9
8
33
32
31
30
29
28
39
38
37
36
35
34
33
32
31
Latitude (°N)
118
120
122
124
Longitude (°E)

**Figure A6.**

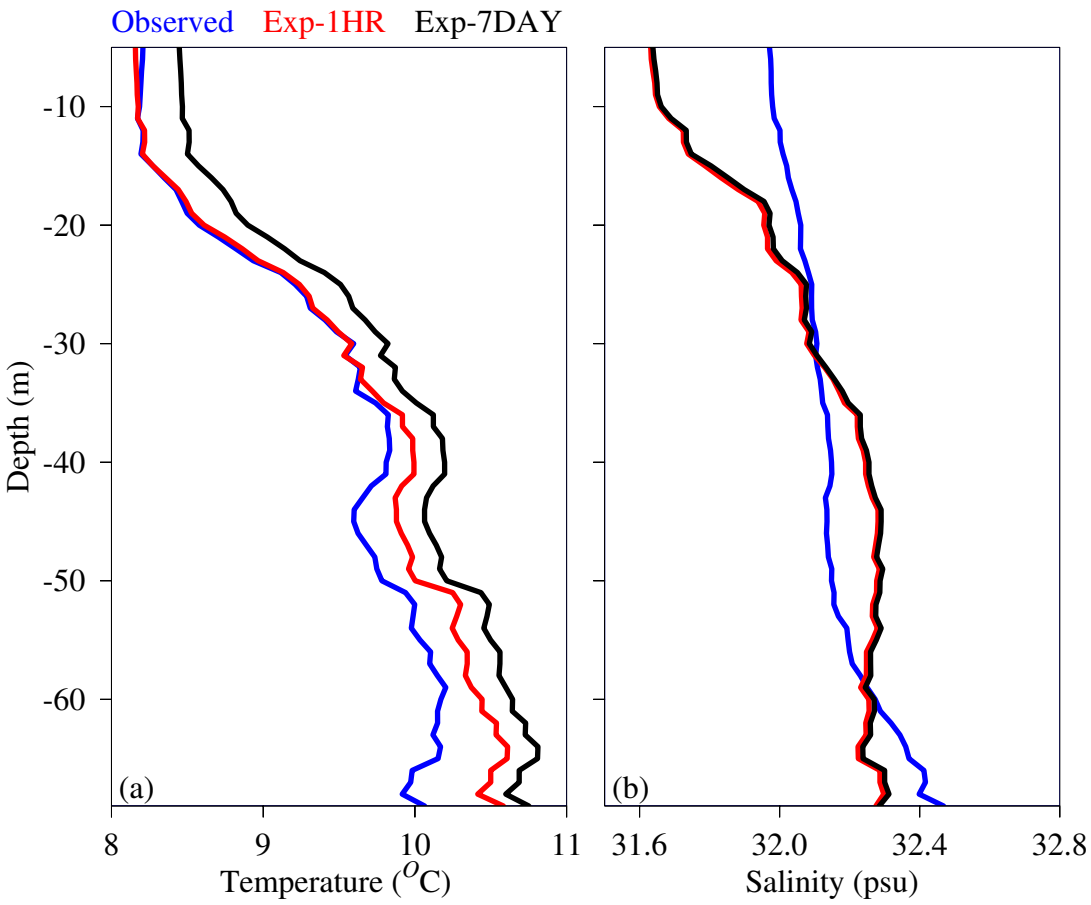
Observed
Exp-1HR
Exp-7DAY
-10
-20
-30
-40
-50
-60
Depth (m)
(a)
(b)
8
9
10
11
Temperature ($^{O}$C)
31.6
32.0
32.4
32.8
Salinity (psu)

## Tables

**Table 1** Information for model experiments

| Exp name | Wind | Pressure | Air Temperature | Relative Humidity | Long wave | Short wave | Heat flux |
|---|---|---|---|---|---|---|---|
| Exp-1HR | 1 hourly wind speed | 1 hourly | 1 hourly | 1 hourly | 1 hourly | 1 hourly | Calculated using bulk formulation |
| Exp-7DAY | 7day running mean wind speed | 7day running mean | 7day running mean | 7day running mean | 7day running mean | 7day running mean | Calculated using bulk formulation |
| Exp-MON | Monthly averaged wind speed | Monthly averaged | Monthly averaged | Monthly averaged | Monthly averaged | Monthly averaged | Calculated using bulk formulation |
| Exp-WIND-MON | Monthly averaged wind speed | 1 hourly | 1 hourly | 1 hourly | 1 hourly | 1 hourly | Calculated using bulk formulation |
| Exp-HEAT-MON | 1 hourly wind speed | Monthly averaged | Monthly averaged | Monthly averaged | Monthly averaged | Monthly averaged | Calculated using bulk formulation |
| Exp-WIND-MON-HEAT-SET | Monthly averaged wind speed | 1 hourly | Not included | Not included | Not included | Not included | Prescribed using net surface flux and short-wave radiation from Exp-1HR |

**Table 2** Lag correlations of sea level elevations between station pairs

| Station pair | Correlation Coefficient | Lag (hours) |
|---|---|---|
| IC-MP | 0.8382 | 1 |
| Bayuquan-MP | 0.7537 | 2 |
| Qinhuangdao-MP | 0.7844 | 4 |
| Tanggu-MP | 0.7630 | 6 |
| Chengshantou-MP | 0.8236 | 8 |
| Rizhao-MP | 0.7452 | 11 |
| Lvsi-MP | 0.7170 | 23 |